A Numerical Study on Mixing and Injection
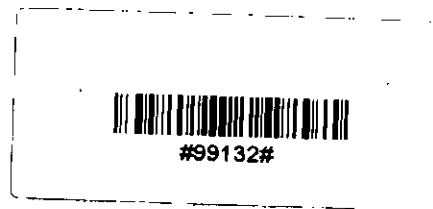## Systems in Supersonic Combustor

by

Md. Rafiqul Hoque

MASTER OF SCIENCE IN MECHANICAL ENGINEERING

DEPARTMENT OF MECHANICAL ENGINEERING

BANGLADESH UNIVERSITY OF ENGINEERING AND TECHNOLOGY

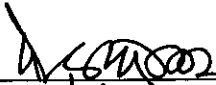Dhaka-1000 , Bangladesh

January 2004.

i

The thesis Titled "**A Numerical Study on Mixing and Injection Systems in Supersonic Combustor**", Submitted by Md. Rafiqul Hoque, Roll No: 100010008 F, Session: October 2000 has been accepted as satisfactory in partial fulfillment of the requirement for the degree of MASTER OF SCIENCE IN MECHANICAL ENGINEERING on 7 January, 2004.

BOARD OF EXAMINERS

Dr. Mohammad Ali
Associate Professor
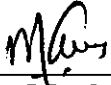Department of Mechanical Engineering
BUET, Dhaka-1000.

Chairman

Dr. Dipak Kanti Das
Professor
Department of Mechanical Engineering
BUET, Dhaka-1000.

Member

Dr. S. M. Nazrul Islam
Professor
Department of Mechanical Engineering
BUET, Dhaka-1000.

Member

Dr. Maglub Al Nur
Professor and Head
Department of Mechanical Engineering
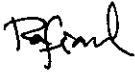BUET, Dhaka-1000.

Member
(Ex- officio)

Dr. Md. Mustafa Kamal Chowdhury
Professor
Department of Mathematics
BUET, Dhaka-1000

Member
(External)

CANDIDATE'S DECLARATION

It is hereby declared that this thesis or any part of it has not been submitted elsewhere for the award of any degree or diploma.

Author

Md. Rafiqul Hoque

Dedicated

To my parents

Contents

Nomenclature

Symbol	Meaning

b	width of injector
h	height of backward-facing step
c	sound speed
C_p	specific heat at constant pressure
D_{iml}	molecular diffusion coefficient of i-th species
D_{it}	turbulent diffusion coefficient of i-th species
D_{ij}	binary-diffusion coefficient for species i and j
E	total energy
F	flux vector in x-direction
$F^{\wedge}$	transformed flux vector in ξ-direction
f_H	local mass fraction of hydrogen
G	flux vector in y-direction
$G^{\wedge}$	transformed flux vector in η-direction
h	enthalpy
H	height of domain [16]
J	transformation Jacobian, number of grid points in x-direction
JJ	maximum number of grid points in x-direction
K	clauser constant, number of grid points in y-direction
KK	maximum number of grid points in y-direction
l	mixing length
M	mach number
$\dot{m}$	mass flux of species
p	pressure
q_c	energy flux by conduction
q_D	energy flux by diffusion
R	universal gas constant
S	Sutherland constant for viscosity
S'	Sutherland constant for thermal conductivity
T	temperature
T_c	effective temperature
t	physical time
U	vector of conservative variables, contravariant velocity in ξ-direction
$U^{\wedge}$	transformed vector of conservative variables
U_i	diffusion velocity of species i
u	horizontal velocity
V	contravariant velocity in η-direction
v	Vertical velocity
W	molecular weight of species
x	horizontal cartesian coordinate
Y	mass fraction of species

y	vertical cartesian coordinate
y^+	low-of-the-wall coordinate
z	mole fraction of species
ξ	transformed coordinate in horizontal direction
η	transformed coordinate in vertical direction
η_m	mixing efficiency
Φ	global equivalence ratio of fuel and oxidizer
ϕ	local equivalence ratio of fuel and oxidizer
θ	injecting angle
ρ	mass density
σ	normal stress
τ	shear stress
μ	coefficient of dynamic viscosity
κ	thermal conductivity
Ω_D	diffusion collision integral
δ	effective collision diameter
ω	vorticity

Superscript

ns	number of species
0	standard state condition

Subscript

a	atmospheric condition
c	index for conduction
D	index for diffusion
i,j	index for species
l	laminar case
m	mixture
t	index for turbulence
v	viscous term
w	wall
x	horizontal direction
y	vertical direction
xy	reference plane
0	reference value, stagnation condition

List of Tables

List of Figures

Acknowledgement

Abstract

A numerical study on mixing of hydrogen injected into a supersonic air stream has been performed by solving Two-Dimensional Navier-Stokes equations. An explicit Harten-Yee Non-MUSCL Modified-flux-type TVD scheme has been used to solve the system of equations, and a zero-equation algebraic turbulence model to calculate the eddy viscosity coefficient.

In this research the mixing characteristics have been investigated for several main flow and side flow inlet parameters. It has been found that recirculation plays an important role to enhance mixing by increasing the gradient of mass concentration. The performance of combustor has been investigated by varying (i) the distance of injector position from left boundary, (iii) the injector angle and (iii) the mach number of the main air stream.

For varying injector distance the results show that the configuration for small distance of injector position has high mixing efficiency but the upstream recirculation cannot evolve properly which is an important factor for flame holding capability. On the other hand, the configuration for very long distance has lower mixing efficiency due to lower gradient of hydrogen mass concentration on the top of injector caused by the expansion of side jet in both upstream and downstream of injector. For moderate distance of injector position large and elongated upstream recirculation can evolve which might be activated as a good flame holder.

For varying injecting angle (taking as anticlockwise) investigation shows that small ($\theta=30^0$) and large ($\theta=120^0$ and 150^0) injecting angles have no significant upstream recirculation. Upstream recirculation is dominant for injecting angle 60^0 and 90^0. Perpendicular injection i.e. injecting angle ($\theta=90^0$) increases both the mixing efficiency and flame holding capability. Small injecting angle ($\theta=30^0$) and very large injecting angle ($\theta=150^0$) have good flame holding capability but not mixing efficiency.

The Mach number of the air stream is changed as (3, 3.25, 3.5, 3.75 and 4). It is found that strong interaction is occurred between the main and injecting flows for higher Mach number (M=4). Higher Mach number increases both the mixing efficiency and flame holding capability. So air stream in supersonic flow having Mach number 4 might act as a good flame holder and become efficient in mixing.

CHAPTER-I
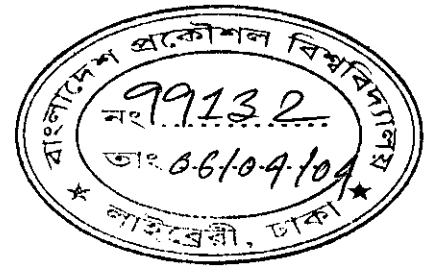
INTRODUCTION

1.1   General

Mixing of fuel with oxidizer and their combustion are encountered in many engineering applications. Particularly, the fuel injection in both supersonic and hypersonic streams requires special attention for efficient mixing and stable combustion. Though a considerable number of researches have been carried out on mixing and combustion of fuel with supersonic air stream, still it faces many unresolved problems. The main problems that arise in this regard, concern mixing of reactants, ignition, flame holding, and completion of combustion. More investigations are required to overcome these problems. In fact, in supersonic combustion, high penetration and mixing of injectant with main stream is difficult due to their short residence time in combustor. In an experimental study, Brown et al. [1] showed that the spreading rate of a supersonic mixing layer decreased drastically with increasing free stream Mach number. A similar conclusion was drawn by Papamoschou et al. [2] on the basis of a theoretical analysis of shear-layers. Furthermore, they showed that the reduction in spreading rate correlated most closely with the convective Mach number, where convective Mach number is defined as the differential velocity normalized by the speed of sound. An independent linear stability theory analysis of Ragab et al. [3] reached the same conclusion. These investigations showed that difficulty exists in achieving a high degree of mixing in high Mach number flows. Therefore, it is necessary to investigate all parameters that affect mixing of hydrogen in supersonic airstream.

There exist several methods of fuel injection in the supersonic air stream. Perpendicular injection causes rapid mixing of injectant with main stream, particularly in upstream portion of the combustor. In this investigation we studied (i) the effect of change of main flow Mach number (ii) the effect of change of injector position from left boundary for a constant Mach number and (iii) the effect of change of injecting angle in a particular injector position and constant Mach number.

1.2   Background

Both experimental and numerical investigations have been performed to analyze the mixing and combustion characteristics, and find out the means of increasing the mixing efficiency. In these investigations the authors showed a number of parameters that can affect on penetration and mixing. In an experiment, Rogers [4] showed the effect of the ratio between jet dynamic pressure and free stream dynamic pressure on the penetration and mixing of a sonic hydrogen jet injected normal to a Mach 4 air stream. In similar flow arrangements, Kraemer et al. [5] found that the relative change in jet momentum (product of gap width, jet static pressure and injectants specific heat ratio) was directly proportional to the relative size between the flowfield disturbance and the upstream separation distance. The downstream injectant penetration height is directly proportional to the upstream separation distance, and, thus, the downstream mixing is dependent on the relative change in jet momentum. Similar conclusions were drawn by Holdeman [6] and Thayer III et al. [7]. Thayer III et al. [7] also found that the injectant concentration of the separated region was high at all conditions investigated. Heister et al. [8] conducted a calculation on the penetration and bow shock shape of a non-reacting liquid jet injected transversely into a supersonic cross flow. Mass and momentum balances were incorporated along the jet with and without the inclusion of mass loss due to droplet shedding. The predicted bow shock position agreed with the data and a correlation was obtained between mass loss, boundary layer thickness, recirculation and related parameters.

Catalano et al. [9] reported the measurements and computations for the turbulent jet discharging into a cross flow confined between two parallel plates. The authors concluded that the jet trajectory and the existence of opposite wall impingement were strongly dependent on the velocity ratio. Zakkay et al. [10] investigated experimentally the interactions of finite-span, transverse jet on a 7° cone with a Mach 5.8 stream. The authors showed that along the plane of symmetry, the separated region upstream of the jet correlated well with the quasi 2-dimensional experiments in terms of the jet penetration. Thayer III [11] performed an experiment showing that the jet interaction flowfield depends markedly on the injectant molecular weight. About the effect of injectant molecular weight on mixing

and penetration of normal jet, Torrence [12] performed an investigation and found that the decay of the maximum value of concentration with axial position was a strong function of injectant molecular weight and the effect on vertical penetration was small. The rate of decay in the far downstream of the injector was similar for all injectants.

Rodriguez et al. [13] showed by his experiment that the mixing zones created by the shock interaction with a discontinuous interface thickened due to turbulent diffusion and became wider than the continuous interface after the second reshock. The separation phenomena of a turbulent boundary layer ahead of a forward-facing were observed by Zukoshi [14] in an experiment without injection. With secondary injection of a gas normal to a supersonic stream, Zukoshi and Spaid [15] investigated the flowfield around the injection port, selected the penetration height as a scaling parameter for correlation of the data. The correlation had some lack of similarity with the observed pressure data in the laminar boundary layer separation region and at the lower mach numbers in the reattachment region downstream of the injector. Weidner et al. [16] conducted a parametric study using staged, perpendicular fuel injectors. They studied the mixing of hydrogen by varying the distance between injectors and the fuel split (percentage of fuel injected per injector). Another numerical investigation on the mixing of side jet into a supersonic flow was performed by Takahashi et al. [17]. The numerical results were compared against the published [16] experimental data, noting that the adoption of higher-class model like a two-equation model was necessary for better prediction. Considering different calculation parameters, a similar flow situation was given by Spaid and Zukoshi [18] with an attempt to correlate the parameters.

Yokota et al. searched the enhancement of mixing by varying (i) the angle of a finite length slit (when slit length is smaller than the width of computational domain) [19] and (ii) slit aspect ratios [20]. Besides, Yokota et al. examined the effects of injection methods [21] and the existence of pressure wave in the flow with the injection [22] on mixing and total pressure loss. Yoshida et al. [23] found out that the ignition of hydrogen injected transversely into the supersonic air stream occurred in the upstream separated region, and the bulk flame produced for downstream of the test section was not essential to the supersonic combustion. Crabb et al. [24] provided an extensive review of earlier works and

3

reported the measurements of the velocity characteristics of a jet in crossflow encompassing the entire mixing region. They confirmed the double vortex characteristics of the downstream flow and demonstrated that it was associated with fluid emanating from the jet. The injector position is another important factor for mixing and combustion. By the numerical investigation of two-dimensional reacting Scramjet engine flowfields, Drummond et al. [25] found that the insufficient penetration of hydrogen reduced the overall reaction in the upstream portion of combustor. They tried to move the injector further upstream (1.3-cm from the engine minimum cross section) which made the engine thermally choked due to severe disturbances produced by injector.

By applying Direct Simulation Monte Carlo (DSMC) method several investigations [26, 27] can be found in literature where Nakae et al. [26] showed that the characteristics of the mixing field agreed with other computed results and Obata et al. [27] found that raising the temperature of the injected hydrogen not only contributed to rapid ignition but also accelerated mixing and diffusion. A numerical study has been performed by Kumar et al. [28] about the techniques for enhancement of turbulence, the ultimate goal of which was to increase the mixing. They found that the wall-region disturbances propagate along the shock, resulting in oscillating shock, which then enhanced turbulence in the main flow. The effect of convective Mach number on the mixing in supersonic shear layer was observed by Guirguis [29]. The result showed the enhancement of mixing when the convective Mach number was reduced. Orth et al. [30] studied in details the interaction and penetration of a supersonic side jet in supersonic external flow both experimentally and numerically. The shape of the side jet was varied. The authors showed that the penetration could be increased by supersonic injection and was weakly affected by injection hole shape. In detailed experimental investigation on the near field (defined as the region of the flow from the jet exit a distance of a few diameters downstream of this exit), Moussa et al. [31] found that the geometric configuration of the boundaries of jet exit plays an important role in the mixing and development process. Some characteristics on boundary layer and turbulence in mixing field were investigated by Andrepoulos et al. [32] and Andreopoulos [33].

1.3   Flow Field Description and Numerical Parameter

The geometric configuration of the calculation domain and the inlet conditions of main and injecting flows are shown in Fig. 1.1(a~b). In all cases, the left boundary of domain consists of a backward facing step of height 5 mm, a main flow inlet of height 1.35-cm and a solid wall of height 3.15 cm. Recirculation has an important role to enhance mixing. A backward-facing step, has been used, which can increase the recirculation region in upstream of injector. The backward facing step of 5 mm has been used because it has been found most efficient in mixing investigated by Ali et al. [41] among the conditions considered. In this study the parameters are injector distance, injecting angle and Mach number of the injector. All the numerical values of the parameters are tabulated in table 3.1. The inlet conditions of hydrogen are used as Weidner et al [16] as shown in Fig 1.1(a~b). We calculate efficiency for Mach number 3, 3.25, 3.5, 3.75 and 4 and observed maximum efficiency for Mach number 4. Using Mach 4 we varied the distance (2, 3, 4, 5 cm) of the injector position from left boundary and observed the maximum efficiency at 2 cm. The inlet widths of air and side jet are used as Ali et al. [43], which showed good performance on mixing. Throughout the study, the grid system consists of 194 nodes in the longitudinal direction and 121 in the transverse direction. The grid system of the calculation flow field is shown in Fig.1.2.

1.4   Objectives

The objective of this research is to study

    i.   Two Dimensional Navier Stokes equations

    ii.   Physics of mixing

    iii.   Enhancement of mixing efficiency

    iv.   Identification of parameter that affect mixing

    v.   Effect of combustor on mixing.

CHAPTER-II

FLOW FIELD MODEL OF SUPERSONIC MIXING

2.1   Governing Equations

The flow field is governed by the unsteady, two-dimensional Navier-Stokes and species continuity equations. The body forces are neglected. With the conservation-law form, Ali et al. can express these equations [40]

$$\frac{\partial U}{\partial t} + \frac{\partial F}{\partial x} + \frac{\partial G}{\partial y} = \frac{\partial F_v}{\partial x} + \frac{\partial G_v}{\partial y}$$

(2.1)

Where

$$U = \begin{pmatrix} \rho \\ \rho u \\ \rho v \\ E \\ \rho Y_i \end{pmatrix}, \quad F = \begin{pmatrix} \rho u \\ \rho u^2 + p \\ \rho u v \\ (E + p)u \\ \rho Y_i u \end{pmatrix}, \quad G = \begin{pmatrix} \rho v \\ \rho u v \\ \rho v^2 + p \\ (E + p)v \\ \rho Y_i v \end{pmatrix}$$

$$F_v = \begin{pmatrix} 0 \\ \sigma_x \\ \tau_{xy} \\ \sigma_x u + \tau_{yx} v - q_x \\ -\dot{m}_x \end{pmatrix}, \quad G_v = \begin{pmatrix} 0 \\ \tau_{yx} \\ \sigma_y \\ \tau_{xy} u + \sigma_y v - q_y \\ -\dot{m}_x \end{pmatrix}$$

$$p = \sum_{i=1}^{ns} \rho_i R_i T = \sum_{i=1}^{ns} \rho_i \frac{R}{W_i} T,$$

(2.2)

$$E = \sum_{i=1}^{ns} \rho_i h_i - \sum_{i=1}^{ns} \rho_i \frac{R}{W_i} T + \frac{\rho}{2} (u^2 + v^2),$$

6

$$E = \sum_{i=1}^{ns} \rho_i \, C_{pi} \, T - \sum_{i=1}^{ns} \rho_i \, \frac{R}{W_i} T + \frac{\rho}{2} \left(u^2 + v^2 \right) \tag{2.3}$$

$$\sigma_x = \lambda \left(\frac{\partial u}{\partial x} + \frac{\partial v}{\partial y} \right) + 2\mu \left(\frac{\partial u}{\partial x} \right), \qquad \sigma_y = \lambda \left(\frac{\partial u}{\partial x} + \frac{\partial v}{\partial y} \right) + 2\mu \left(\frac{\partial v}{\partial y} \right),$$

$$\tau_{xy} = \tau_{xy} = \mu \left(\frac{\partial u}{\partial y} + \frac{\partial v}{\partial x} \right), \qquad \lambda = -\frac{2}{3} \mu \tag{2.4}$$

Mass diffusion occurs whenever there exists a gradient in the proportions of the mixture, i.e. a concentration gradient. Because of this gradient, there is a mass motion of species, i in the opposite direction. If the velocity of this mass motion is U_i, called the diffusion velocity, the mass flux of species, i is $\rho_i U_i$. This mass flux is given approximately by Fick's law [34] as

$$\dot{m} = \rho_i U_i = -\rho D_{iml} \nabla Y_i \tag{2.5}$$

Where ρ is the mixture density and D_{iml} is the molecular diffusion coefficient of species, i for diffusion into the mixture. The density of mixture is determined from

$$\rho = \sum_{i=1}^{ns} \rho_i \tag{2.6}$$

Due to heat conduction, the flux of energy,

$$q_c = -\kappa \nabla T \tag{2.7}$$

And due to diffusion, energy flux of the species,

$$q_D = \sum_{i=1}^{ns} \rho_i U_i h_i \tag{2.8}$$

Therefore, the total energy flux (radiation is neglected),

$$q = -\kappa \nabla T + \sum_{i=1}^{ns} \rho_i U_i h_i \tag{2.9}$$

Considering the flowfield with gradients of temperature and mass fractions in x- and y-directions, the total energy flux in x-direction can be obtained by Eq. (2.9) as

$$q_x = -\kappa \frac{\partial T}{\partial x} + \sum_{i=1}^{ns} \rho_i U_{i_x} h_i \qquad (2.10)$$

Where U_{ix} is the component of diffusion velocity of species, i in x-direction. From Eq. (2.5), we can write

$$\rho_i U_{ix} = -\rho D_{iml} \frac{\partial Y_i}{\partial x} \qquad . \qquad (2.11)$$

Combining Eq. (2.10) and (2.11), we get

$$q_x = -\kappa \frac{\partial T}{\partial x} - \rho \sum_{i=1}^{ns} D_{iml} h_i \frac{\partial Y_i}{\partial x} \qquad (2.12)$$

Similarly, the total energy flux in y-direction

$$q_y = -\kappa \frac{\partial T}{\partial y} - \rho \sum_{i=1}^{ns} D_{iml} h_i \frac{\partial Y_i}{\partial y} \qquad (2.13)$$

Moreover, from Eq. (2.5), we can write the mass flux of species, i in x-direction caused by diffusion as

$$\dot{m}_x = -\rho D_{iml} \frac{\partial Y_i}{\partial x} \qquad (2.14)$$

and in y-direction

$$\dot{m}_y = -\rho D_{iml} \frac{\partial Y_i}{\partial y} \qquad (2.15)$$

8

The specific heat and enthalpy of the mixture are determined from the following expressions:

$$C_p = \sum_{i-1}^{ns} Y_i \, C_{pi} \tag{2.16}$$

$$h = \sum_{i=1}^{ns} Y_i \, h_i \tag{2.17}$$

Where C_{pi} and h_i are the specific heat and enthalpy of the i-th species.

The values of C_{pi} and h_i are considered as functions of temperature and are determined from the polynomial curve fitting developed by Moss [35]. They are as follows:

$$\frac{C_{pi}}{R_i} = a_{1i} + a_{2i}T + a_{3i}T^2 + a_{4i}T^3 + a_{5i}T^4 \tag{2.18}$$

$$\frac{h_i}{R_i T} = a_{1i} + \frac{a_{2i}T}{2} + \frac{a_{3i}T^2}{3} + \frac{a_{4i}T^3}{4} + \frac{a_{5i}T^4}{5} + \frac{a_{6i}}{T} \tag{2.19}$$

Where a_1 to a_6 are constants for different species. The coefficients for these curve are found in Table 2.1. Two sets of coefficients are available in Table 2.1 of which one for temperature range 0 ~ 1000 K, the other set for 1000 ~ 5000 K.

2.2   Calculation of Temperature

Temperature is calculated by Newton-Raphson method. By rearranging Eq. (2.3), a relation for temperature can be expressed as

$$F(T) = \sum_{i=1}^{ns} \rho_i \, h_i - \sum_{i=1}^{ns} \rho_i \frac{R}{.W_i} T + \frac{\rho}{2}\left(u^2 + v^2\right) - E \tag{2.20}$$

Substituting the value of h_i from Eq. (2.19), Eq. (2.20) can be written as

$$F(T) = b_0 + b_1 T + b_2 T^2 + b_3 T^3 + b_4 T^4 + b_5 T^5 \tag{2.21}$$

Where the coefficients are

$$b_0 = \sum_{i=1}^{ns} \rho_i R_i a_{6i} + \frac{\rho}{2}\left(u^2 + v^2\right) - E, \quad b_1 = \sum_{i=1}^{ns} \rho_i R_i a_{6i} - \sum_{i=1}^{ns} \rho_i R_i$$

$$b_2 = \frac{1}{2}\sum_{i=1}^{ns} \rho_i R_i a_{2i} \qquad b_3 = \frac{1}{3}\sum_{i=1}^{ns} \rho_i R_i a_{3i} \qquad (2.22)$$

$$b_4 = \frac{1}{4}\sum_{i=1}^{ns} \rho_i R_i a_{4i} \qquad b_5 = \frac{1}{5}\sum_{i=1}^{ns} \rho_i R_i a_{5i}$$

Differentiating Eq. (2.21) with respect to T, we get

$$F'(T) = b_1 + 2b_2 T + 3b_3 T^2 + 4b_4 T^3 + 5b_5 T^4 \qquad (2.23)$$

Then the temperature is calculated by the following equation:

$$T_{new} = T_{old} - \frac{F(T_{old})}{F'(T_{old})} \qquad (2.24)$$

The calculation of Eq. (2.24) is repeated until it fulfils the criterion for the temperature T_{new}. The criterion for this calculation is $|(T_{new} - T_{old})| < 1.0$.

2.3 Transport Coefficients

The transport properties; the viscosity coefficient μ and thermal conductivity κ of individual species are determined from Sutherland formulae [36] as

$$\frac{\mu_i}{\mu_{i0}} = \left(\frac{T}{T_{i0}}\right)^{1.5} \frac{T_{i0} + S_i}{T + S_i} \qquad (2.25)$$

$$\frac{\kappa_i}{\kappa_{i0}} = \left(\frac{T}{T_{i0}}\right)^{1.5} \frac{T_{i0} + S_i'}{T + S_i'} \qquad (2.26)$$

Where S_i and S_i' are the Sutherland constants, while μ_{i0}, T_{i0} and κ_{i0} are the reference values of i-th species. These constants are taken from References 36 and 37 and are also tabulated in Table 2.2. Once the viscosity coefficient and thermal conductivity of each species are determined, the mixture viscosity and thermal conductivity are determined by Wilke's formula [36] and Wassiljewa's equation [38], respectively as

$$\mu_l = \sum_{i=1}^{ns} \frac{z_i \, \mu_i}{\sum\limits_{j=1}^{ns} z_j \, \phi_{ij}}$$

(2.27)

$$\kappa_l = \sum_{i=1}^{ns} \frac{\kappa_i}{1 + \frac{1}{z_i} \sum\limits_{\substack{j=1 \\ j \neq i}}^{ns-1} A_{ij} Z_j}$$

(2.28)

Where $\phi_{ij} = \dfrac{\left[1.0 + \left(\mu_i / \mu_j\right)^{0.5} \left(W_j / W_i\right)^{0.25}\right]^2}{\left(8 + 8W_i / W_j\right)^{0.5}}$, $A_{ij} = 1.065\, \phi_{ij}$, z_i, and z_j are the mole fractions

of i-th and j-th species, respectively.

The molecular-binary-diffusion coefficient for i-th and j-th species, D_{ij} is determined from the empirical formula given by Chapman-Cowling [36] as

$$D_{ij} = \frac{0.002858\, T^{1.5} \left(\dfrac{W_i + W_j}{W_i \, W_j}\right)^{0.5} x 10^{-4}}{P \sigma_{ij}{}^2 \, \Omega_D}$$

(2.29)

Where $\Omega_D = \left(\dfrac{T}{T_{\varepsilon i}}\right)^{-0.145} + \left(\dfrac{T}{T_{\varepsilon i}} + 0.5\right)^{-2.0}$

(2.30)

$T_{\varepsilon ij} = \left(T_{\varepsilon i}\, T_{\varepsilon j}\right)^{0.5}$

(2.31)

$\sigma_{ij} = \dfrac{1}{2}\left(\sigma_i + \sigma_j\right)$

(2.32)

T = absolute temperature (K)

P = pressure (atm).

Values of the effective temperature $T_{\varepsilon i}$ and effective collision diameter, σ_i of i-th species are taken from References [36] and [38], are also tabulated in Table 2.2. Using the value of

11

binary diffusion coefficient, the effective molecular diffusion coefficient for each species is determined by the following formula given in Reference [38] as

$$D_{iml} = \frac{1 - Z_i}{\sum\limits_{\substack{j=1 \\ j \neq i}}^{ns-1} Z_j / D_{ij}}$$

(2.33)

2.4   Numerical Scheme

The system of governing equations has been solved, using an explicit Harten-Yee Non-MUSCL Modified-flux-type TVD scheme [39]. The scheme is second order accurate in time and space. The two-dimensional, rectangular physical coordinate system (x,y) is transformed into the computational coordinate system (ξ,η) in order to solve the problem on uniform grids. The details of the transformation procedure can be found in Reference [40]. After applying the transformation, Eq. (2.1) can be expressed as

$$\frac{\partial \hat{U}}{\partial t} + \frac{\partial \hat{F}}{\partial \xi} + \frac{\partial \hat{G}}{\partial \eta} = \frac{\partial \hat{F}_v}{\partial \xi} + \frac{\partial \hat{G}_v}{\partial \eta}$$

(2.34)

Where $\hat{U} = J^{-1} U$

$$\hat{F} = J^{-1} \left(\xi_x F + \xi_y G \right), \qquad\qquad \hat{G} = J^{-1} \left(\eta_x F + \eta_y G \right)$$
$$\hat{F}_v = J^{-1} \left(\xi_x F_v + \xi_y G_v \right), \qquad\qquad \hat{G}_v = J^{-1} \left(\eta_x F_v + \eta_y G_v \right)$$

(2.35)

The transformation Jacobian J and grid metric terms are

$$J^{-1} = X_\xi Y_\eta - X_\eta Y_\xi, \qquad \xi_x = J y_\eta, \ \xi_y = J x_\eta,$$
$$\eta_x = -J Y_\xi, \qquad \eta_y = -J x_\xi$$

(2.36)

The time step for calculation is determined by

$$\Delta t = \frac{CFL}{\max\{|U| + |V| + c \, (\xi_x^2 + \xi_y^2)^{1/2} + c \, (\eta_x^2 + \eta_y^2)^{1/2}\}}$$

(2.37)

12

Where the Courant number CFL is chosen as 0.7 to obtain rapid convergence and avoid unsteadiness in calculation. The contravariant velocities are

$$U = \xi_x u + \xi_y v, \qquad V = \eta_x u + \eta_y v \qquad (2.38)$$

2.5 Boundary Conditions and Convergence Criterion

A Navier-Stokes analysis imposes that the normal and tangential velocity components are zero on the walls. The walls are assumed to be thermally adiabatic, so that $(\partial T / \partial n)_w = 0$. For non-catalytic walls, the normal derivative of species mass fraction also vanishes, and consequently the gradient of total density becomes zero. The pressure is determined from the equation of state. The temperature, pressure and density at inflow boundary are assumed steady. At the outflow boundary the variables are determined by first-order extrapolation due to supersonic character of flow. Throughout the present study, the following convergence criterion has been set on the variation of density:

$$\sqrt{\frac{\sum\limits_{J=1,K=1}^{JJ.KK} \left(\dfrac{\rho_{new} - \rho_{old}}{\rho_{old}}\right)^2}{JJ.KK}} \leq 10^{-5} \qquad (2.39)$$

Where JJ and KK are the total numbers of nodes in the horizontal and vertical directions respectively.

2.6 Use of Turbulence Model

Throughout the investigation the backward -facing step makes the flowfield turbulent at the present Mach number. Particularly, the recirculations in both upstream and downstream of injector, shocks and expansion of both main stream and side jet leads us to use a turbulence model. Therefore, to calculate eddy viscosity we selected the zero equation turbulence model. A zero-equation algebraic turbulence model developed by Baldwin and Lomax is used to simulate boundary layer separation, recirculation and shock-expansion regions near the injector. The model is patterned with modifications that avoid the necessity for finding the edge of the boundary layer. This has been very helpful because at the injection port and

adjacent region it is difficult to define boundary layer thickness. According to the model the eddy viscosity μ_t is defined as

$$\mu_t = \begin{cases} (\mu_t)_{inner} & y \le y_{crossover} \\ (\mu_t)_{outer} & y > y_{crossover} \end{cases} \qquad (2.40)$$

where y is the normal distance from the wall and $y_{crossover}$ is the smallest value of y at which the value of viscosity in the outer region becomes less than or equal to the value of viscosity in the inner region.

The viscosity in the inner region is given by

$$(\mu_t)_{inner} = \rho \, l^2 \, |\omega| \qquad (2.41)$$

The mixing length in the inner region l is expressed as

$$l = ky \left[1 - \exp(-y^+ / A^+) \right] \qquad (2.42)$$

where

$$y^+ = \frac{\rho_w \, u_\tau \, y}{\mu_w} = \frac{\sqrt{\rho_w \, \tau_w} \, y}{\mu_w} \qquad (2.43)$$

For two-dimensional flow, the magnitude of the vorticity is given by

$$|\omega| = \sqrt{\left(\frac{\partial u}{\partial y} - \frac{\partial v}{\partial x} \right)^2} \qquad (2.44)$$

For the outer region,

$$(\mu_t)_{outer} = K \, C_{CP} \, \rho \, F_{WAKE} \, F_{KLEB}(y) \qquad (2.45)$$

where K is the Clauser constant, C_{CP} an additional constant, and

$$F_{WAKE} = \min\left\{ (y_{max} F_{max}), \, \left(C_{wk} y_{max} U_{dif}^2 / F_{max} \right) \right\} \qquad (2.46)$$

Here F_{max} is the maximum value of the function

$$F(y) = y|\omega| \left[1 - \exp(-y^+ / A^+) \right] \qquad (2.47)$$

at each y station in the flow domain, and y_{max} is the y coordinate at which this maximum occurs. The function $F_{KLEB}(y)$ is the Klebanoff intermittency factor given by

$$F_{KLEB}(y) = \left[1 + 5.5 \left(\frac{C_{KLEB}\, y}{y_{max}} \right)^6 \right]^{-1} \tag{2.48}$$

U_{dif} is the difference between the magnitude of the maximum and minimum total velocity in the profile at a fixed x station, expressed as

$$U_{dif} = \left(\sqrt{u^2 + v^2} \right)_{max} - \left(\sqrt{u^2 + v^2} \right)_{min} \tag{2.49}$$

where $\left(\sqrt{u^2 + v^2} \right)$ is taken to be zero along all x station.

The outer formulation (Eqs. 2.12 and 2.13) can be used in wakes as well as in attached and separated boundary layer. The product $y_{max}F_{max}$ replaces $\delta^* u_e$ in the Clauser formulation and the combination $y_{max}U_{dif}^2/F_{max}$ replaces δU_{dif} in a wake formulation. In effect, the distribution of vorticity is used to determine length scales so that the necessity for finding the outer edge of the boundary layer is removed.

The following are the constants used for this model and are directly taken from Baldwin and Lomax (1978):

$A^+ = 26$,	$C_{CP} = 1.6$,	$C_{KLEB} = 0.3$,
$C_{wk} = 0.25$,	$k = 0.4$,	$K = 0.0168$

The values of the turbulent thermal conductivity of the mixture κ_t and turbulent diffusion coefficient of i-th species D_{it} are obtained from eddy viscosity coefficient μ_t by assuming a constant turbulent Prandtl and Lewis number equal to 0.91 and 1.0, respectively. They can be expressed as

$$\frac{\mu_t Cp}{k_t} = 0.91 \tag{2.50}$$

$$\frac{\rho\, D_{it} Cp}{k_t} = 1.0 \tag{2.51}$$

The final values of μ, κ and D_{im} used in the governing equations are

$$\mu = \mu_l + \mu_t \tag{2.52}$$

$$\kappa = \kappa_l + \kappa_t \tag{2.53}$$

$$D_{im} = D_{iml} + D_{it} \tag{2.54}$$

3. Program verification

To verify the present code, a comparison has been made with the experimental data published by Weidner et al. [16]. The geometry of the experiment is shown in the inset on Fig. 2.1, where helium was injected at sonic condition from a 0.0559 cm slot into a rectangular duct 25.4 cm long and 7.62 cm high. The slot was located 17.8 cm downstream of the duct entrance. The flow conditions of helium at the slot exit were P = 1.24 MPa, T = 217.0 K and M = 1.0. At the entrance of the duct, the air stream conditions were P = 0.0663 MPa, T = 108.0 K and M = 2.9. Using the same geometry and flow conditions we computed the flow field with a grid system consisting of 246 x 165 nodes in the horizontal and vertical directions, respectively. At the exit of the injector 10 nodal points are used.

Fig. 2.1 shows that the computed pressure along the bottom wall agrees well with the experiment in both the upstream and downstream of the injector. Both show a pressure rise in the upstream separated region and downstream reattachment region. An over-prediction can be found at the immediate downstream of the injector where the turbulence is naturally intensified by the disturbance caused by the injector. Fig. 2.2 gives the static pressure distribution along the vertical axis at 3.81 cm downstream of the injector. Qualitatively, the computed pressure profile agrees with the experimental data. Small variation on the position of recompression shock and bow shock, and the pressures at these positions can be observed in the computation. In the experiment, the recompression shock occurs at y/H = 0.2 (H is the height of domain), whereas in computation at 0.16. After recompression, both show a linear increase of pressure. The calculation determines the similar difference in the position of bow shock as that of recompression shock. In the experiment the position of bow shock is at y/H = 0.63, while in computation it is 0.59. Beyond the bow shock, the calculation shows the similar decreasing rate of pressure with experiment. Fig. 2.3 shows the comparison between the mass fraction profiles of injected helium along the same vertical axis at 3.81 cm downstream of the injector. The computed curve agrees with the experimental data at all points along the vertical axis. The computation shows that the overall computed results agree with the experiment in spite of the complexities of injected flow field. The code is therefore considered to be adequate for application to calculate the mixing flow fields.

CHAPTER-III

RESULTS AND DISCUSSION

3.1 Introduction

The performance of combustor has been investigated by varying (i) the mach number of the main stream (ii) the distance of injector position from the entrance of main flow (iii) the injector angle. The findings are analyzed and discussed under the following subsections.

3.2 Effect of Injector Distance

3.2.1 The Physics of Fluid Dynamics

The physics of flow is important to understand the penetration and mixing of hydrogen which is the interest of this study. Figures 3.1(a~d) show velocity in both upstream and downstream of injector. Strong interaction occurs between the main and injecting flows shown in Figure 3.1(a) for case 1. The strength of interaction can be understood from the slope of velocity vectors at the top of injector. For long distance of injector position both main and injecting flows lose their strength due to viscous action and upstream recirculations. There are two recirculations in upstream of the injector observed in figure 3.1 (b~d). In case 2 due to small space in upstream, two very small recirculations (one is primary and the other is secondary) exist. With the increase in distance of injector in case 3 and 4 the recirculations are increasing in areas and the primary one expands towards the left though the pattern of expansion is different. In case 1, recirculations are not strong and the upstream region is seems to be stagnant, whereas cases 2 ~ 4 have strong recirculations due to wide space in upstream. In downstream two features are to be mentioned; (i) no strong recirculation exists in any case, and (ii) for small distance of injector, the injecting jet is bent sharply into downward direction caused by strong interaction between main and injecting flows. Another observation is that with the increase in distance of injector position, the expansion of injecting jet plume increases. This is caused by the loss of strength of main flow and early separation of boundary layer.

3.2.2 Penetration and Mixing of Hydrogen

Figure 3.2(a~d) shows the penetration and mass concentration of hydrogen in the flow field. There are various definitions of penetration in literature. In this paper the term "penetration" is referred to the edge of mixing region in the vertical direction where the mole fraction of hydrogen is 5%. Accordingly, Figure 3.2(a~d) shows that there is little difference in penetration at both upstream and downstream of the configurations. Two competing phenomena are activated in this regard; (i) due to strong interaction in small distance of injector, high gradient of hydrogen mass concentration exists causing high penetration of hydrogen, and (ii) in longer distance of injector, large and elongated upstream recirculation causes high penetration dominated by convection of recirculation. The mass concentration of hydrogen in upstream and that in downstream can be explained separately. For small distance of injector, most of the upstream region contains high concentration of hydrogen. It can be pointed out that the flame holding requires longer residence time of flame in the burning range and this residence time strongly depends on the geometric expansion of the recirculation zone [44]. Also the equivalence ratio of fuel and oxidizer in mixture is an important factor for burning because among the mixtures, the stoichiometric strength is good for combustion. Therefore, longer recirculation zone containing stoichiometric mixture strength results in a longer residence time and leads to a more stable flame. The cases having injector distance 20 mm, 30 mm and 40 mm can produce larger and elongated upstream recirculation where most of the region contains good proportion of hydrogen and oxygen (mole fraction is about 0.4~0.7) exists. Again in case 4 having injector distance 50 mm, far upstream contains lower mass concentration of hydrogen which is not good for flame holding. This uniform distribution of hydrogen is caused by higher expansion of side jet. However, the uniform distribution does not mean higher mixing efficiency. The performance of different cases is evaluated by calculating mixing efficiency. Figure 3.3 shows mixing efficiency along the length of physical model for different Cases. Mathematically, the mixing efficiency is defined by

$$\eta_m = \frac{\int_A \left(f_H \, \rho \bar{u} \, d\bar{A} \right) / \phi'}{\dot{m}_H / \Phi}$$

18

Where,

A = arbitrary section plane

f_H = local mass fraction of hydrogen

ρ = total density

$\vec{u}$ = velocity vector

$d\vec{A}$ = small area normal to velocity vector

$\dot{m}_H$ = total mass flux of hydrogen

ϕ' = local equivalence ratio = $\begin{cases} 0.25 & \phi' < 0.25 \\ \phi' & \phi' \geq 0.25 \end{cases}$

Φ = global equivalence ratio = $\begin{cases} 0.25 & \Phi < 0.25 \\ \Phi & \Phi \geq 0.25 \end{cases}$

In the flow field where large amount of hydrogen is present with negligible amount of oxygen, the calculation of mixing efficiency is avoided by dividing the large value of ϕ'. On the other hand, where a very small amount of hydrogen is present, an error in calculation of mixing efficiency can be occurred by the small value of ϕ'. This error has been eliminated by setting the minimum value of $\phi' = 0.25$ which corresponds to the lower flammability limit. It can be pointed out that similar expression for mixing efficiency was used by Yokota et al [19~20]. In this investigation, the global equivalence ratio Φ for all cases is 2. Figure 3.3 shows mixing efficiency along the length of physical model for different cases. Figure shows that mixing efficiency increases very sharply at injector position of respective cases. Generally, in upstream region, the increasing rate of mixing is moderate and in downstream it is very slow. Individually, case 1 has the highest increment of mixing efficiency at injector position due to strong interaction of main and injecting flows as discussed earlier. Besides, case 4 shows that in upstream the overall mixing efficiency is lower (about 14.7%) than the other cases. The mixing efficiency of case 2 is higher than that of cases 3 ~ 4 on the top of injector. In downstream, the increasing rate of mixing is slower for all cases caused by the supersonic nature of flow. However, among the cases investigated, case 1 has the maximum increasing rate of mixing in downstream.

3.2.3 Characteristics of the Flow Field

The characteristics of the flow field are shown in Figs. 3.4(a~d) and 3.5(a~d). Characteristic phenomena such as separation shock, bow shock, Mach disk, reattachment shock can be seen in Figs. 3.4(a~d) and 3.5(a~d). Figure 3.4 shows the pressure contours by which the pressure distribution and different shocks of other cases can be understood. Flow separation is initiated by the backward-facing step at left boundary. The main flow is deflected upward by the existence of wall at the upper part of the left boundary. The deflection angle decreases with the increase of injector distance caused by weak interaction. The under expanded side jet rapidly expands and forms a Mach disk and a bow shock due to the interaction with main flow. The size of Mach disk increases with the increase of injector distance 'd' caused by higher expansion of side jet. The maximum pressure in the flow field rises about 2.56×10^6 Pa immediately behind the intersection of separation shock and bow shock, where as the temperature rises about 2198 K at the same position. In the downstream region the reattachment shock is more visible in the pressure contour of Fig. 3.4. The pressure is higher in the upstream recirculation region while it is much lower immediately behind the injector caused by the suction of injection.

3.3 Effect of Injecting angle

3.3.1 The Physics of Fluid Dynamics

Figures 3.6 (a~e) show the velocity vector in both upstream and downstream of injector. In upstream there is a pair of large and small recirculation. For case 5 the recirculations are not dominant. With the increase of injector angle the recirculations are observed clearly (case 6 ~7) and again for further increase of injector angle (case 8~9) they are not significant. The large primary clockwise recirculation is caused by the backward facing step and the secondary small counter clockwise recirculation close to injector is caused by the primary recirculation and the suction of injection. The primary recirculation increases the boundary layer thickness and therefore the injection into a thick boundary layer creates greater penetration, resulting in higher mixing. Due to the interaction between main flow and side jet, the velocity of the main flow is slowed down and air enters the upstream recirculation. On the other hand by diffusion and convection due to injection, the injected hydrogen enters the recirculation and mixes well with air. So upstream recirculations play a vital role on

20

mixing and consequently case 7 and 8 show better mixing. In down stream there is no strong recirculation in any case. Case 7 shows a very small recirculation in the downstream of injector caused by the suction of the injection and bending of the side jet. This recirculation and convection due to injection immediately downstream of the injector cause better mixing in case 7.

3.3.2 Penetration and Mixing of Hydrogen

Figures 3.7 (a~e) show the penetration and mass concentration of hydrogen in the flow field. Penetration and mixing of hydrogen can occur by means of (i) turbulence and convection due to recirculation and velocity of the flow, (ii) molecular diffusion. For all cases (case 5 ~ 9) the mole fraction contours of hydrogen are concentrated in a narrow region on the top of the injector, which might become a high heat release zone in the reacting flow field. The backward facing step associated with upstream recirculation brings the injected hydrogen up to the left boundary in all cases. The hydrogen penetration height at different downstream locations can also be compared from Fig 3.7 (a~e). As stated earlier that the flame holding requires longer residence time of flame in the burning range and this residence time strongly depends on the geometric expansion of the recirculation zone. Therefore, longer recirculation zone containing stoichiometric mixture strength results in a longer residence time and leads to a more stable flame. Accordingly case 7 ($\theta=90^{\circ}$) and 8 ($\theta=120^{\circ}$) have good flame holding capability, because they can produce larger and elongated upstream recirculation where most of the region contains good proportion of hydrogen and oxygen. Again in cases having $\theta = 30^{\circ}$ and 150° upstream region contains lower mass concentration of hydrogen which is not good for flame holding. Figure 3.8 shows the mixing efficiency along the length of physical model for different cases (case 5~9). Mathematically, the mixing efficiency is defined earlier. Physically mixing efficiency indicates the ratio of hydrogen mass flow rate capable of burning to its total mass flow rate at the exit of sidejet. Figure 3.8 shows that mixing efficiency increases sharply at injector position of respective cases. Generally, in upstream region, the increasing of mixing is moderate and in downstream it is very slow. Individually, case 7 ($\theta=90^{\circ}$) and 8($\theta=120^{\circ}$) have the highest increment of mixing efficiency at injector position due to strong upstream recirculation. In downstream the increasing rate of mixing along the length of physical model for case 7

21

($\theta=90°$) is higher than case 8 ($\theta=120°$) whereas for case 9 ($\theta=150°$) it remains almost constant which indicates that for case 9, the larger combustor might increase the cost of construction of combustor provided the other parameters are identical. So case 7 ($\theta=90°$) has the maximum increasing rate of mixing in downstream.

3.3.3   Characteristics of the flow field

The characteristics of the flow field are shown in figs. 3.9 and 3.10 (a~e). For case 7 ($\theta=90°$) the pressure in the downstream is relatively lower, at upper part of the flow field. Various characteristic phenomena such as separation shock, bow shock, Mach disk, reattachment shock can be seen in figure 3.9 (a~e) and 3.10 (a~e). Figure 3.9 (a~e) shows the pressure contours by which the pressure distribution and different shocks can be understood. Flow separation is initiated by the backward facing step at left boundary. The main flow is deflected upward by the existence of wall at the upper part of the left boundary. The deflection angle first increases with the increase of injecting angle and then decreases for further increase of injecting angle. The deflection angle is maximum for case 7 ($\theta=90°$) caused by strong interaction. The under expanded side jet rapidly expands and forms a Mach disk and a bow shock due to the interaction with main flow. This increasing Mach disk is caused by higher expansion of side jet. For the injecting angle $\theta=90°$ the slope of the bow shock is steeper indicating high interaction between the main and sidejet. Due to strong interaction, high gradient of mass concentration exists and this indicates more uniform mixing. The maximum pressure and temperature in the flow field rises immediately behind the intersection of separation shock and bow shock. In the downstream region the reattachment shock is more visible in the pressure contour of figure 3.9 (a~e). The reattachment shock starts more or less at the same point for all cases (case 5~9). The pressure is higher in the upstream recirculation region while it is much lower immediately behind the injector caused by the suction of injection. Figure 3.10 (a~e) shows the temperature contours of cases (7~9). Among the all cases the maximum temperature rises in case 7 (about 2368 K) (where pressure 1.1×10^6 Pa) immediately behind the intersection of separation shock and bow shock. It is also clear from the Fig. 3.10 that the interaction between the main and the side flow is maximum in case 7. Other characteristics such as separation shock and Mach disk can also be understood from the Fig. 3.10.

22

3.4   Effect of Mach number of the Air Stream

3.4.1   Penetration and Mixing of Hydrogen

Figures 3.11 (a~e) show the penetration and mass concentration of hydrogen in the flow field. Different penetration height can be found at both upstream and downstream for different cases. Case 10~11 contain good penetration of hydrogen and oxygen in upstream recirculation region, but penetration height is low. For high Mach number (case 12~14), large and elongated upstream recirculation causes high penetration dominated by convection of recirculation. At the same time due to strong interaction, high gradient of hydrogen mass concentration exists causing high penetration of hydrogen. It can be pointed out that the increase of Mach number causes higher penetration of hydrogen. This can be explained by the fact that the increase of Mach number decreases the air inlet pressure which helps the expansion of side jet resulting in high penetration.

Figure 3.12 shows the mixing efficiency along the length of physical model for different cases (case 10~14). The figure shows that mixing efficiency increases sharply at injector position for all cases. Generally in upstream region, the increasing rate of mixing is moderate and in downstream it is slow. Individually, case 14 (Mach 4) has the highest increment of mixing efficiency both at the upstream region and injector position due to strong upstream recirculation and high interaction between air stream and side jet. Again case 14 shows that in upstream the increment of mixing along the length of physical model is the highest, whereas in downstream the increment of mixing is slow and almost equal for all cases caused by the supersonic nature of flow. On the top of injector the increment of mixing efficiency of case 14 is higher than cases 10~13. Including the effects activated for mixing, case 14 has the highest overall mixing efficiency at the outflow boundary.

3.4.2   Characteristics of the flow field

The characteristics of the flow field are shown in Figs 3.13(a~e) and 3.14 (a~e) . Various characteristics such as separation shock, bow shock, Mach disk, reattachment shock can be seen in figure 3.13 (a~e) and 3.14 (a~e). Figure 3.13 (a~e) shows the pressure contours by which the pressure distribution and different shocks can be understood. Flow seperation is

initiated by the backward facing step at left boundary. The deflection angle of air stream increases with the increase of Mach number caused by the decrease of air inlet pressure. The under expanded side jet rapidly expands and forms a Mach disk and a bow shock due to the interaction with main flow. For high Mach number the slope of the bow shock is steeper indicating strong interaction between the main and side jet resulting in the high gradient of mass concentration and consequently higher mixing efficiency. The maximum pressure and temperature in the flow field rises immediately behind the intersection of seperation shock and bow shock. In the downstream region the reattachment shock is more visible in the pressure contour as shown in Fig. 3.13 (a~e). The pressure is higher in the upstream recirculation region while it is much lower immediately behind the injector caused by the suction of injection. Fig.3.14 (a~e) shows the temperature contours for the cases (Case 10~14). The maximum temperature, found for cases 10, 11, 12, 13 and 14 are 2233 , 2335, 2467, 2561 and 2698 K, respectively. It can be pointed out that case 14 has the highest temperature which is caused by the interaction of side jet with high momentum (Mach 4) of main flow. The separation shock, bow shock and Mach disk can also be understood from Fig.3.14 (a~e). The temperature is lower at the upper point of the flow field for all cases and at the upper left corner the temperature is lowest.

CHAPTER-IV

CONCLUSION

4.1   Summary of the study

A numerical study on the mixing of hydrogen in supersonic airstream has been studied by solving two-dimensional Navier-Stoke equations. The ultimate goal of this study is to increase mixing efficiency and flame holding capability. It was found that in supersonic combustion, high penetration and mixing of fuel with oxidizer is difficult due to their short residence time in combustor. Therefore, it is necessary to analyze and find out the means of increasing mixing efficiency.

This study is completed with several investigations. Here we have reported (i) the effect of change of Mach number (ii) the effect of change of injector position (iii) the effect of change of injecting angle of the injector on mixing of hydrogen with air. As an injectant, gaseous hydrogen is used because it is the most suitable fuel and has high potential of heat release. This is why, a considerable number of researchers [4, 15, 16, 18 ~ 21, 24] have performed their investigations using hydrogen as an injectant. For the present investigation, the Mach numbers used were varied as (3, 3.25, 3.5, 3.75, 4) without changing the position (30mm) of the injector from the left boundary. Then the position of the injector was varied as 20, 30, 40 and 50 mm respectively from left boundary. Finally, the injecting angle was varied as (30°, 60°, 90°, 120°, 150°) anticlockwise by placing the injector 30 mm from the left boundary. The purpose of this variation of parameters was to search the configuration of a supersonic combustor, which can increase the penetration, and mixing of gaseous hydrogen into an air stream.

It may be noted out that most of the previous researchers used infinite parallel flow configuration for investigations about penetration and mixing of side jet. But the finite parallel flow configuration shows higher penetration, more uniform distribution and rapid mixing of hydrogen and that is why it has been used finite flow configuration in all investigations.

For varying Mach number of the main stream it is found that strong interaction occurs between the main and injecting flows for higher Mach number (M=4). Higher Mach number increases both the mixing efficiency and flame holding capability. Pressure loss decreases with the increase of Mach number. So mainstream having Mach number 4 might act as a good flame holder and become efficient in mixing.

It has been found that in case of varying injector distance, strong interaction occurs between the main and injecting flows for small distance of injector position. For long distance of injector position both main and injecting flows lose their strength due to viscous action and upstream recirculation. Small distance of injector position does not have strong recirculation but long distances have strong recirculations due to wide space in upstream. The small distance of injector position increases the mixing efficiency but decreases the flame holding capability. The pressure loss increases with the increase of injector distance. In conclusion, the range of setting the injector is from 20~30mm, the configuration might act as a good flame holder and become efficient in mixing. For very long distance of injector position (40mm or more), the configuration reduces both the mixing efficiency and flame holding capability.

For varying injector angle (taking anticlockwise), the investigation shows that small and large injecting angles increase the flame holding capability but decrease mixing efficiency. For moderate injecting angle, the configuration has high mixing efficiency and forms large recirculations in upstream of injector, which might act as a good flame holder.

4.2   Recommendations for Future study

A good supersonic combustor requires efficient mixing. But efficient mixing is difficult due to supersonic nature of flow. Moreover flame holding capability is also an important factor for a supersonic combustor. Though many researchers devoted themselves to overcome these problems. The present investigation has considered some parameters to analyze their effects on mixing and flame holding capability. Still it needs more investigations considering other geometric configurations.

In this investigation, zero equation turbulence model has been used. This turbulence model has an advantage because it does not need to calculate the boundary layer thickness for determining the eddy viscosity. A two-equation model i.e. K-ϵ model can be used to see the effects of different parameters on mixing flow field particularly the recirculation region.

Table 2.1 Coefficients of Thermodynamic Polynomials

Temperature range from 0 ~ 1000 K		
Coefficients	H_2	N_2
a_1	0.33553514E+01	0.37044177E+01
a_2	0.50136144E-03	-0.14218753E-02
a_3	-0.23006908E-06	0.28670392E-05
a_4	-0.47905324E-09	-0.12028885E-08
a_5	0.48522585E-12	-0.13954677E-13
a_6	-0.10191626E+04	-0.10640795E+04
Temperature range from 1000 ~ 5000 K		
Coefficients	H_2	N_2
a_1	0.30667095E+01	0.28532899E+01
a_2	0.57473755E-03	0.16022128E-02
a_3	0.13938319E-07	-0.62936893E-06
a_4	-0.25483518E-10	0.11441022E-09
a_5	0.29098574E-14	-0.78057465E-14
a_6	-0.86547412E+03	-0.89008093E+04

Table 2.2 Constants used in Transport Equations

Species	$T_{i0}(K)$	Viscosity		Thermal conductivity		Molecular Diffusion		
		$\mu_{i0} \times 10^6$ kg/(m.s)	$S_i(K)$	k_{i0} W/(m.K)	$S_i'(K)$	W gm/mol	$\sigma_i(A)$	$T_{\varepsilon i}(K)$
H_2	273	8.41	96.67	0.16273	166.67	2.0159	2.827	59.7
Air	273	17.16	110.06	0.02415	194.44	28.996	3.711	78.6

Table 3.1 Calculation Summary

Calculation Parameters	Computational Runs				
Injector distance	20mm Case-1	30mm Case-2	40mm Case-3	50mm Case-4	
Injecting angle	30^0 Case-5	60^0 Case-6	90^0 Case-7	120^0 Case-8	150^0 Case-9
Mach No.	3 Case-10	3.25 Case-11	3.5 Case-12	3.75 Case-13	4 Case-14
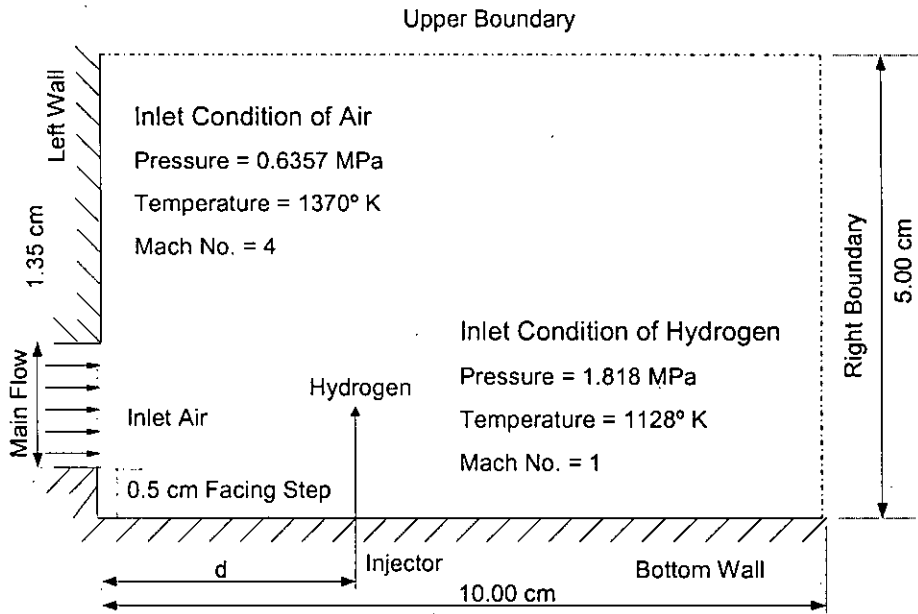
Fig. 1.1(a) Schematic with numerical parameters for varying injector position (d = 20, 30, 40, 50 mm)
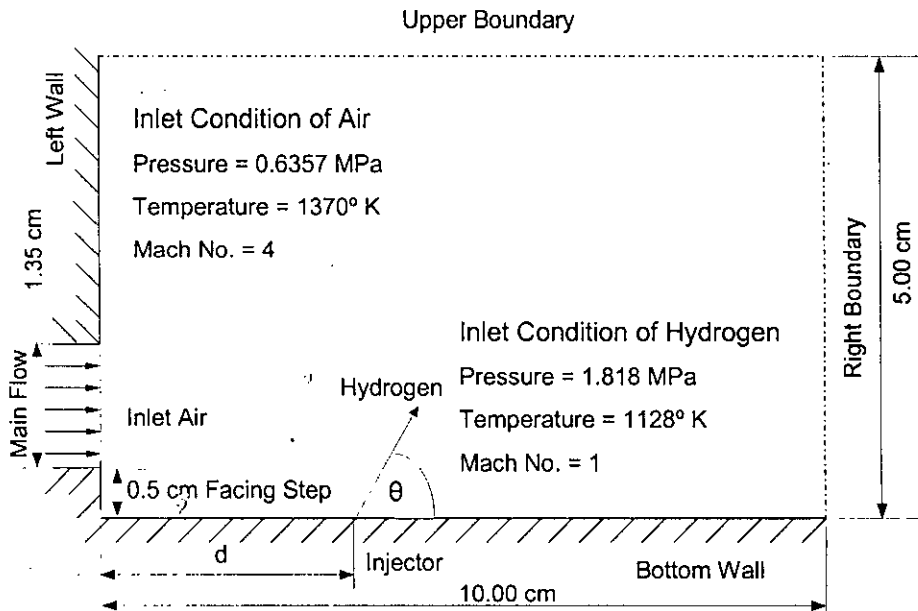
Fig. 1.1(b) Schematic with numerical parameters for varying injector angle (θ = 20°, 30°, 40°, 50°)
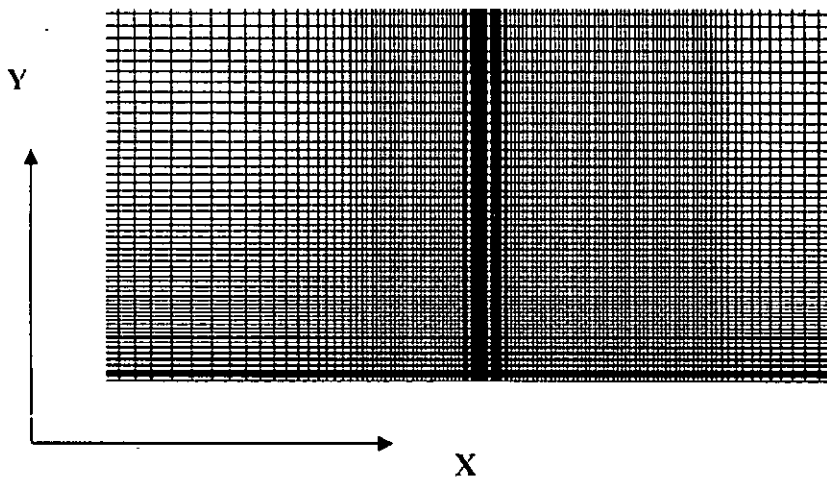
Fig.1.2 Grid system of the calculation flow field
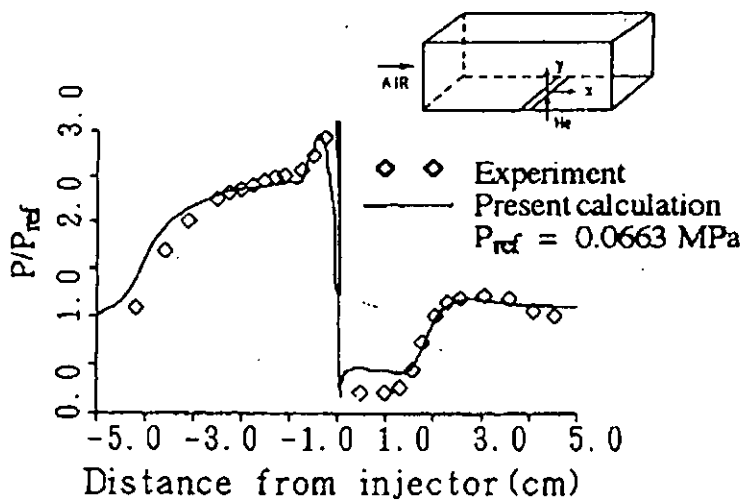
Fig. 2.1 Comparison between experimental and computed pressures along bottom wall (where Helium is injected at 90° angle).
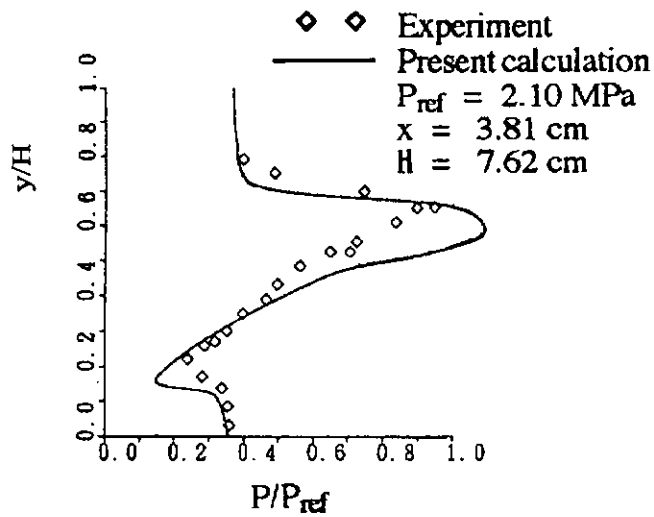
Fig. 2.2 Comparison between experimental and computed pressures at 3.81 cm downstream of injector.
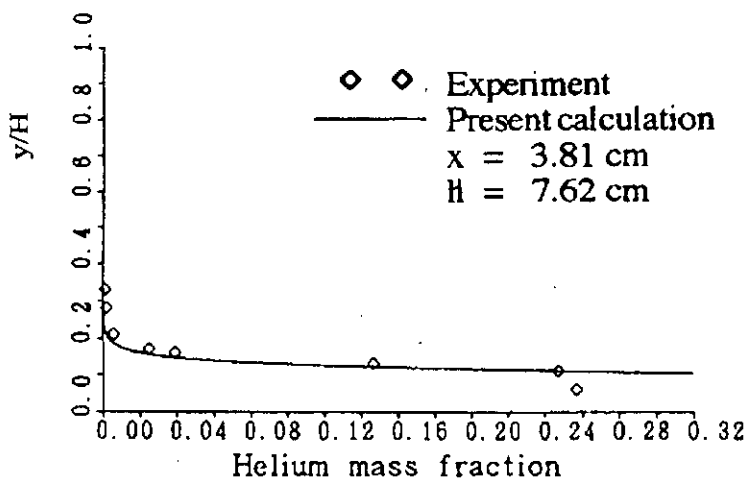
Fig. 2.3 Comparison among helium mass fraction at 3.81 cm downstream of injector.
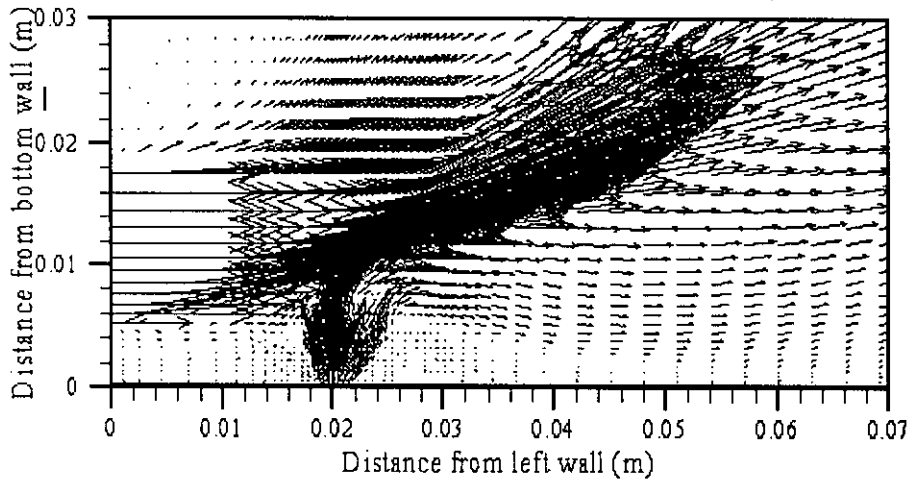
Fig. 3.1 (a) Velocity vector near injector; Case-1 (d=20 mm)
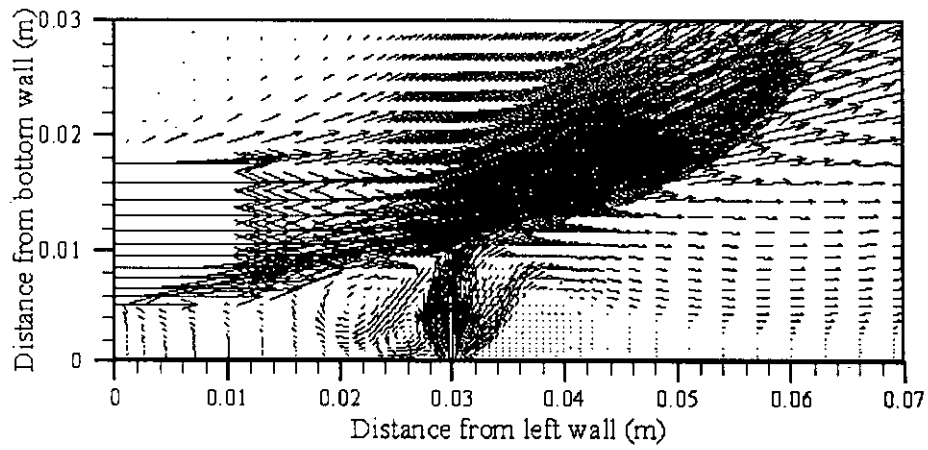
Fig. 3.1 (b) Velocity vector near injector; Case-2 (d=30 mm)
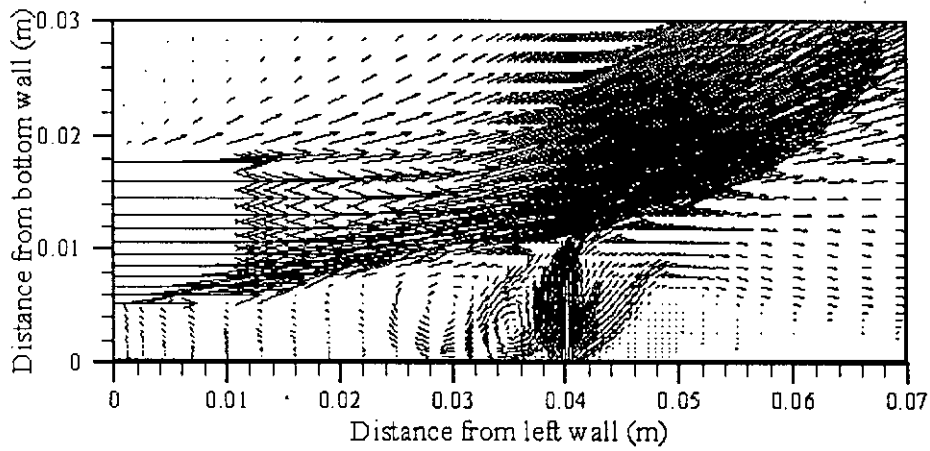
Fig. 3.1 (c) Velocity vector near injector; Case-3 (d=40 mm)
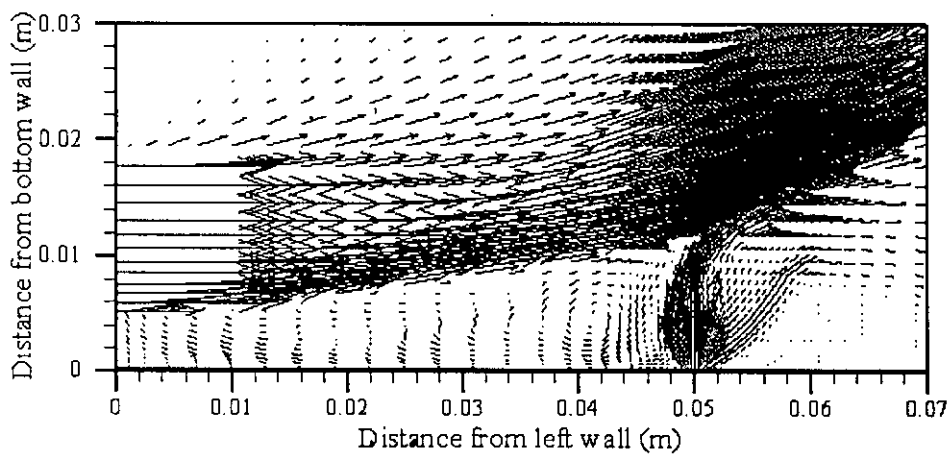
Fig. 3.1 (d) Velocity vector near injector; Case-4 (d=50 mm)

34
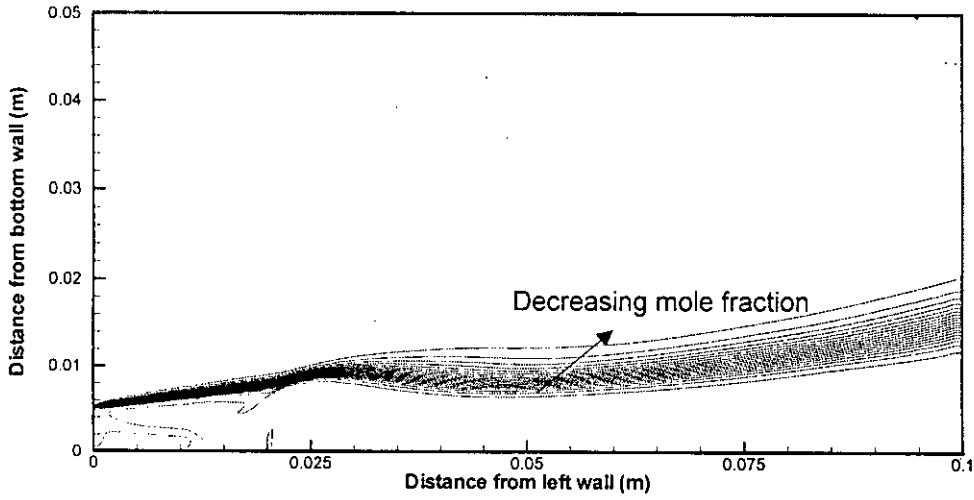
Fig. 3.2(a) Mole fraction counter of Hydrogen, $\Phi(0.05, 1.0, 0.05)$; Case-1(d=20mm)
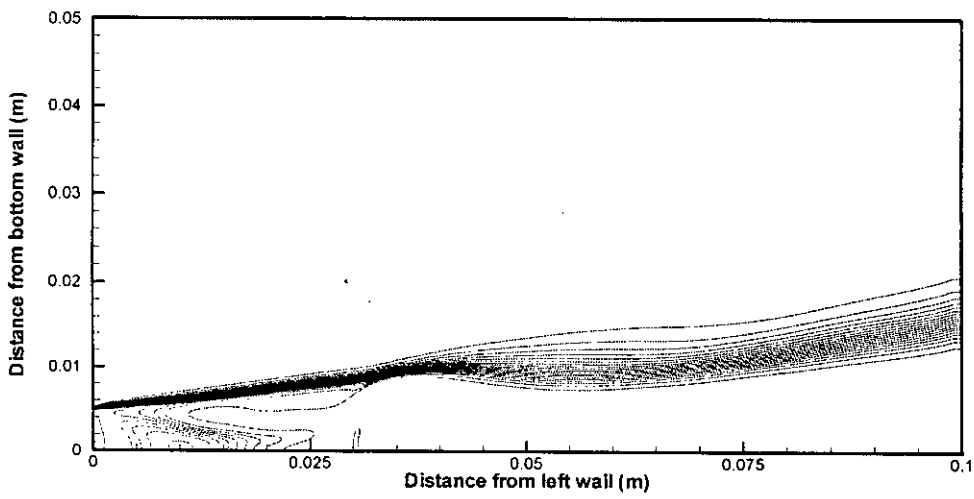
Fig. 3.2(b) Mole fraction counter of Hydrogen, $\Phi(0.05, 1.0, 0.05)$; Case-2(d=30mm)

35
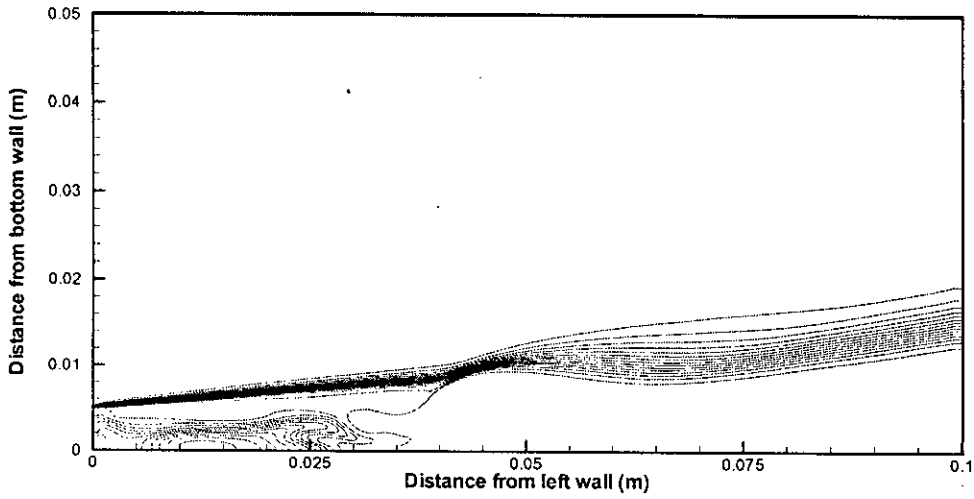
Fig. 3.2(c) Mole fraction counter of Hydrogen, $\Phi(0.05, 1.0, 0.05)$; Case-3(d=40mm)
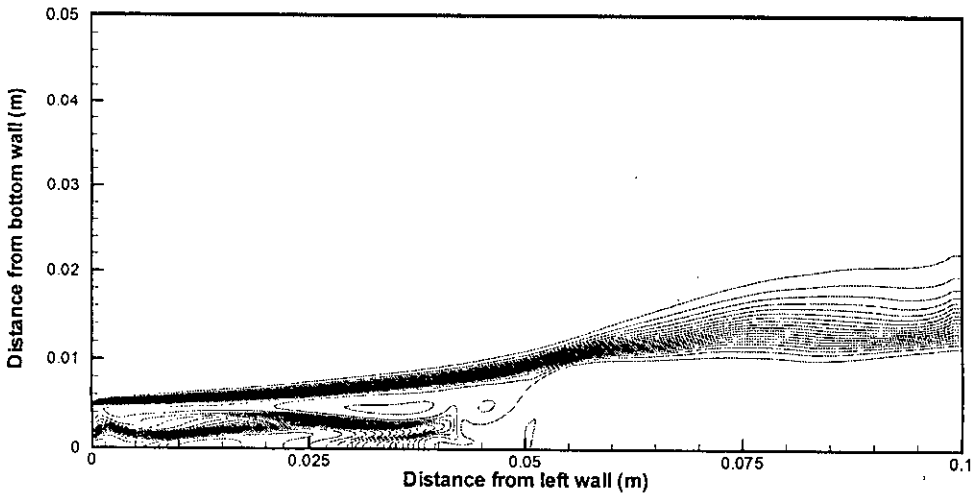
Fig. 3.2(d) Mole fraction counter of Hydrogen, $\Phi(0.05, 1.0, 0.05)$; Case-4(d=50mm)
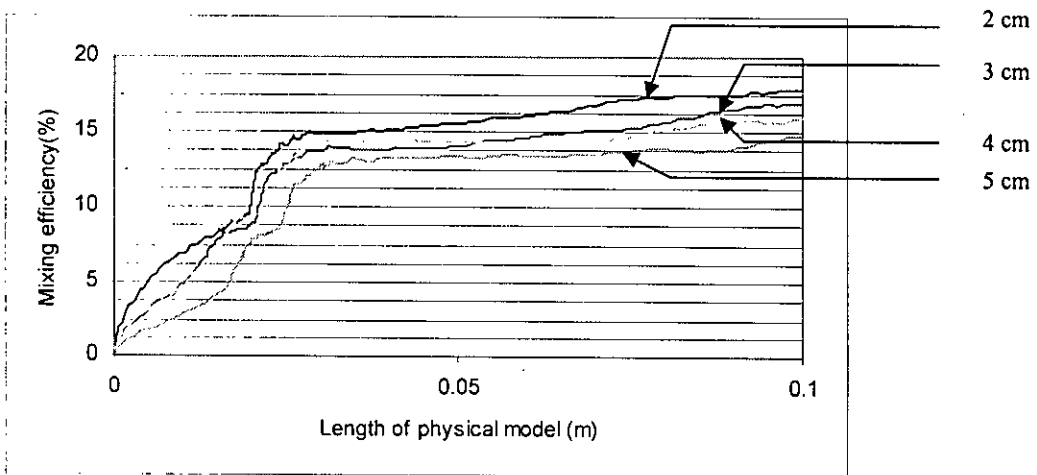
Figure 3.3 Mixing efficiency along the length of physical model
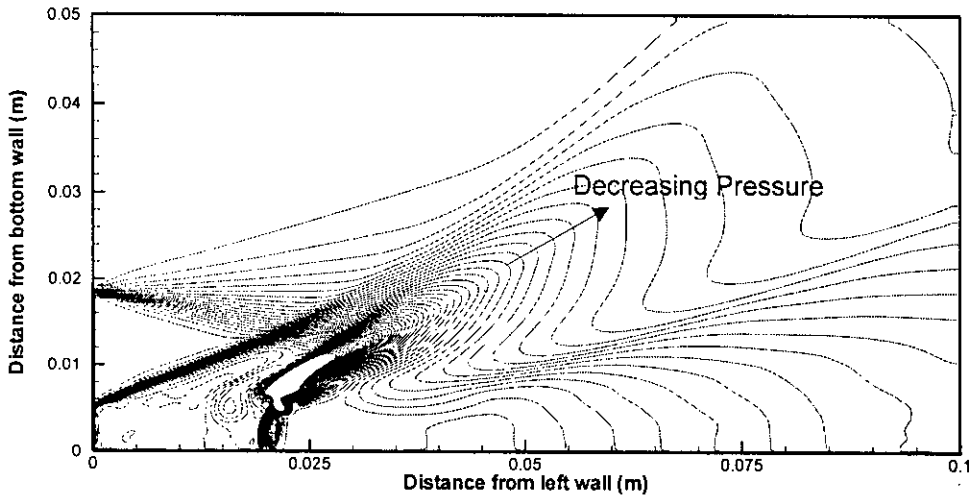
Fig. 3.4(a) Pressure (Pa) contour, $\Phi(2*10^4, 2*10^6, 2*10^4)$; Case-1(d=20mm)
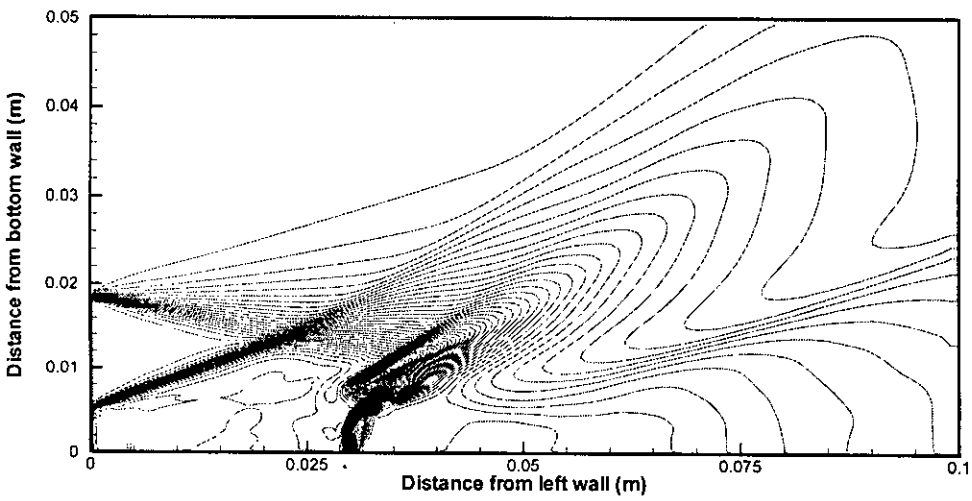
Fig. 3.4(b) Pressure (Pa) contour, $\Phi(2*10^4, 2*10^6, 2*10^4)$; Case-2(d=30mm)
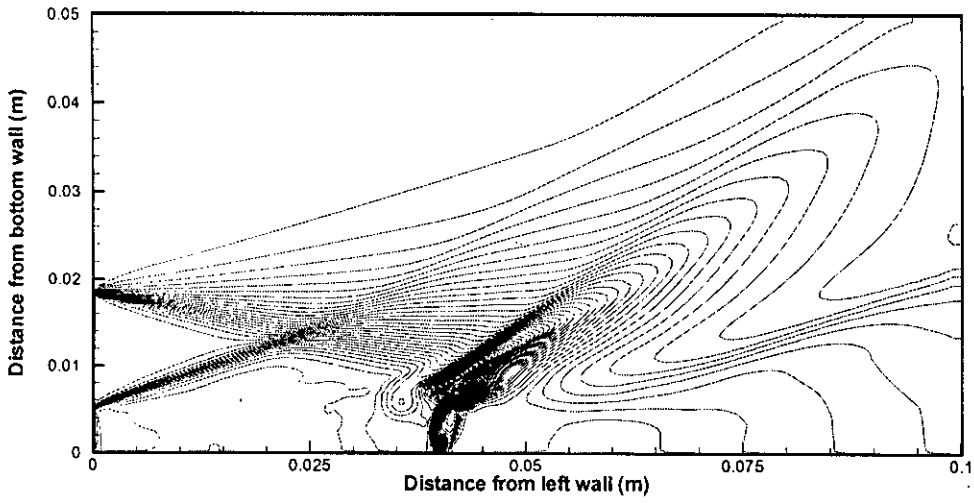
Fig. 3.4(c) Pressure (Pa) contour, $\Phi(2*10^4, 2*10^6, 2*10^4)$; Case-3(d=40mm)
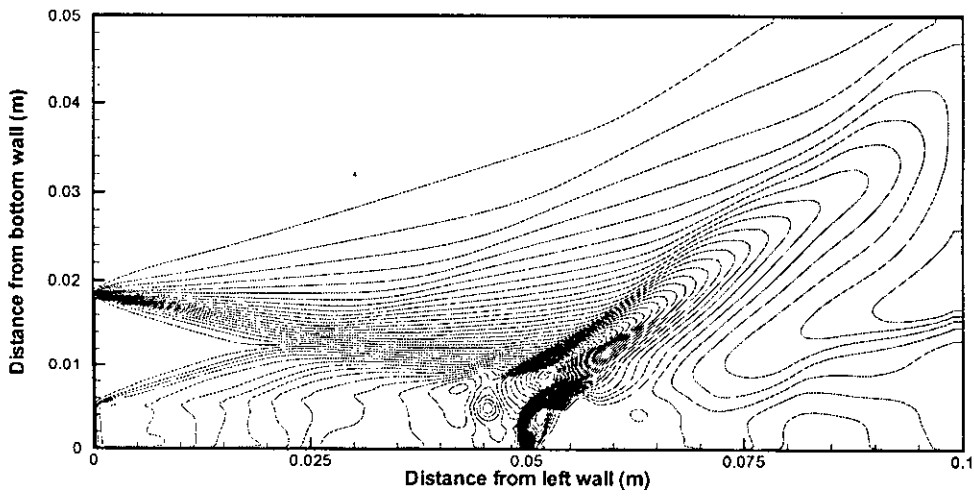
Fig. 3.4(d) Pressure (Pa) contour, $\Phi(2*10^4, 2*10^6, 2*10^4)$; Case-4(d=50mm)
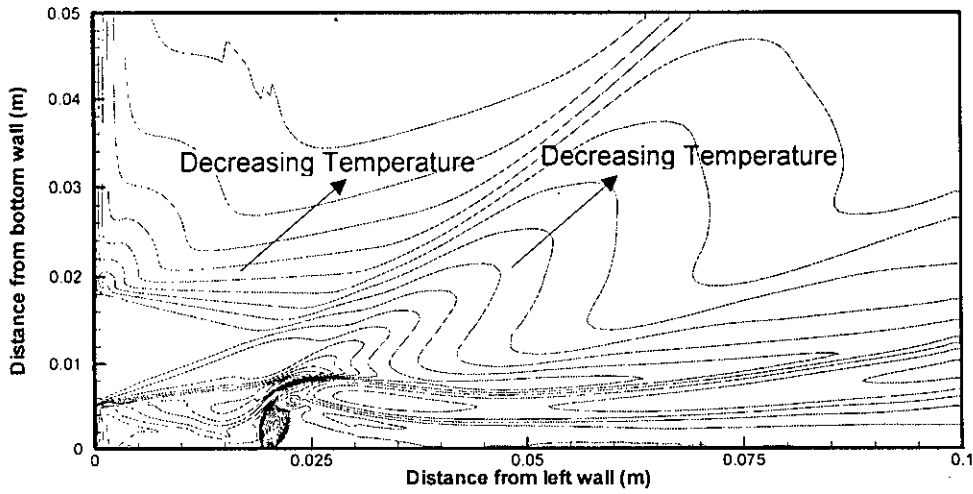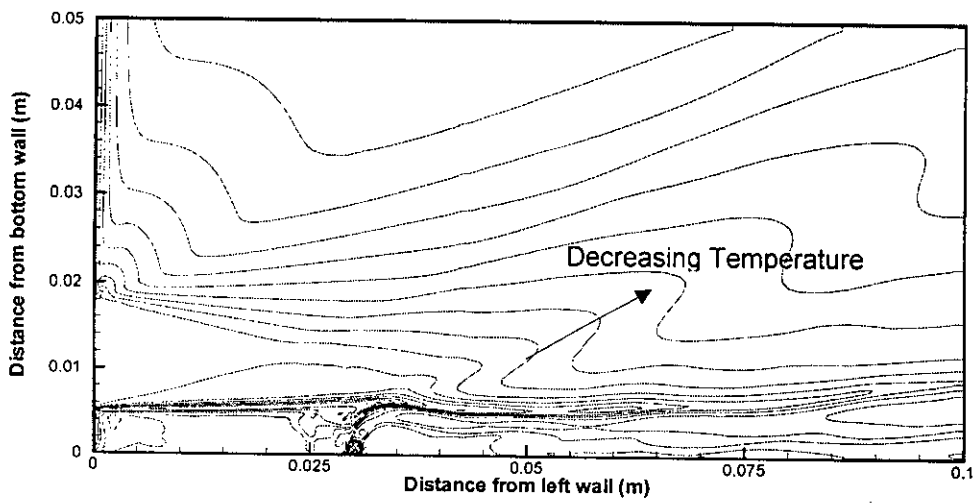
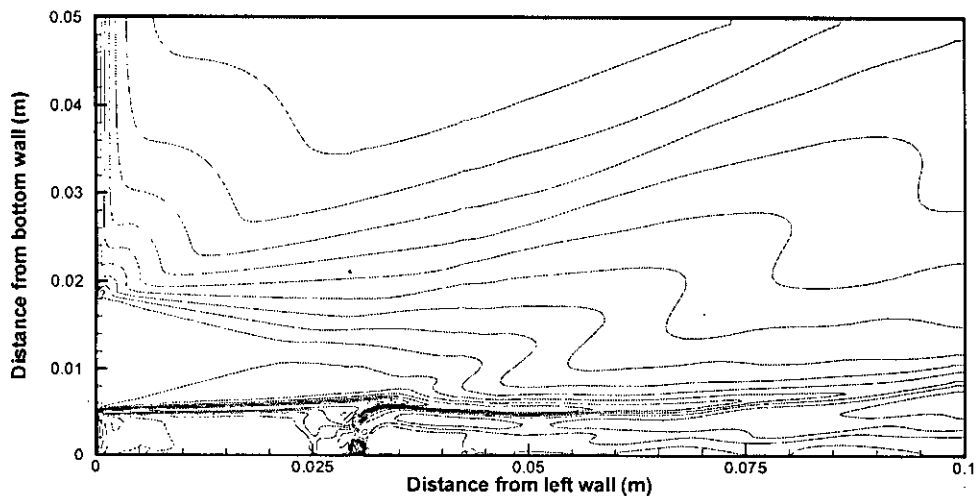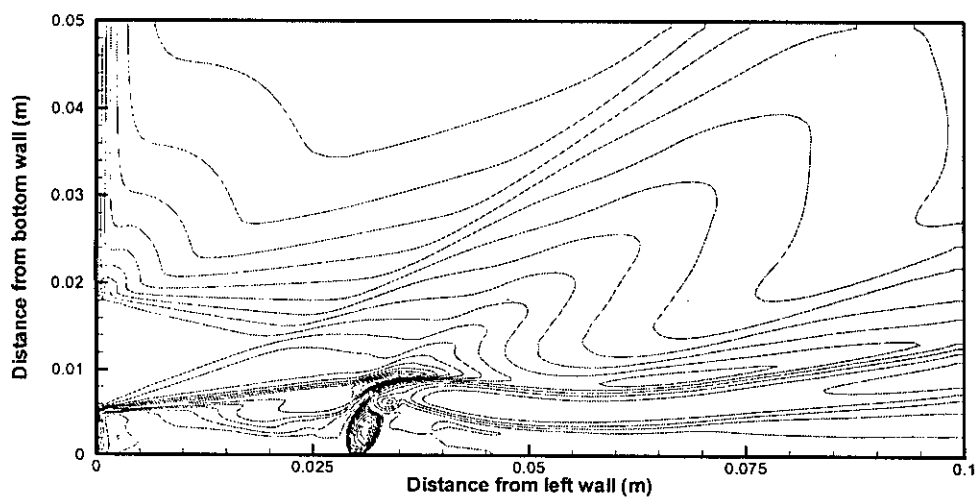Fig. 3.5(a) Temperature (K) contour, $\Phi(250, 2550, 100)$; Case-1(d=20mm)
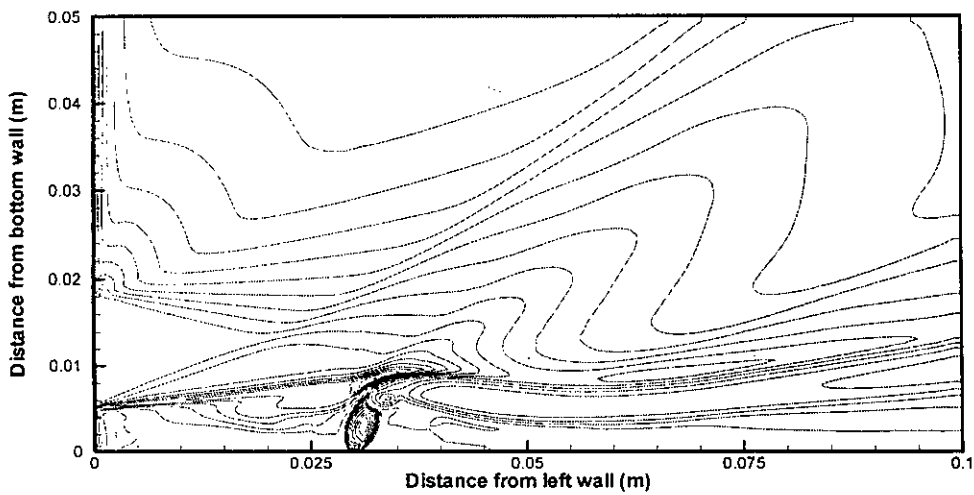
Fig. 3.5(b) Temperature (K) contour, $\Phi(250, 2550, 100)$; Case-2(d=30mm)
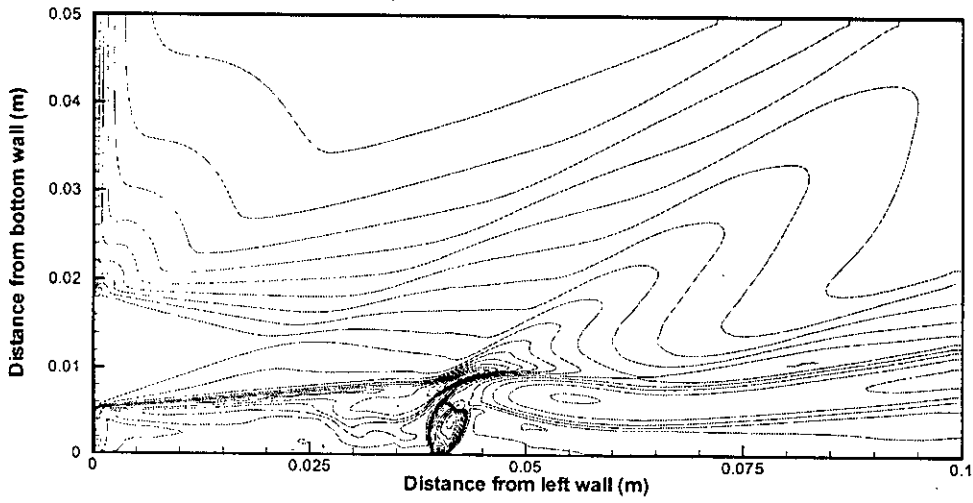
Fig. 3.5(c) Temperature (K) contour, Φ(250, 2550, 100); Case-3(d=40mm)
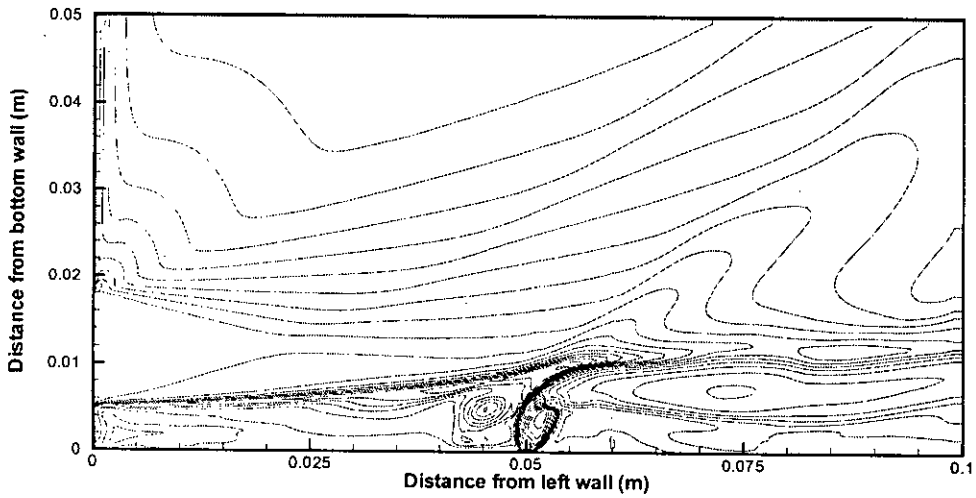
Fig. 3.5(d) Temperature (K) contour, Φ(250, 2550, 100); Case-4(d=50mm)
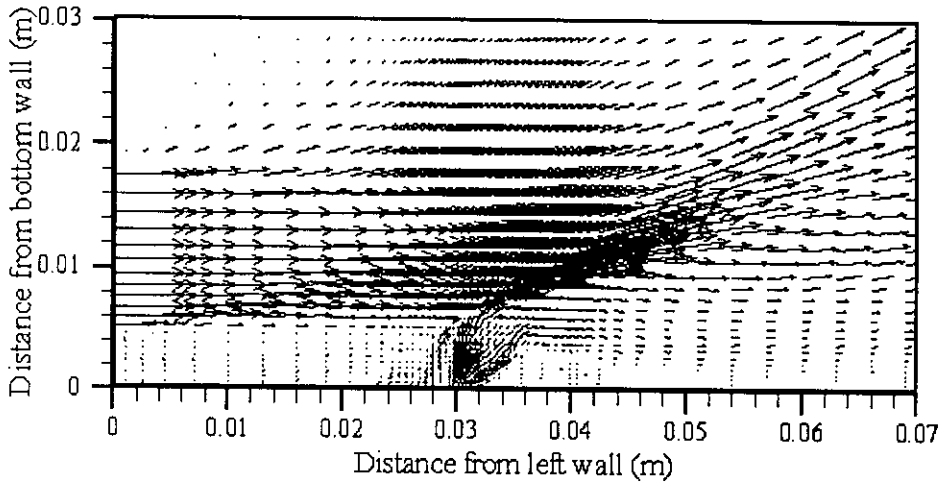
Fig. 3.6 (a) Velocity vector near injector; Case-5 ($\theta = 30^0$)
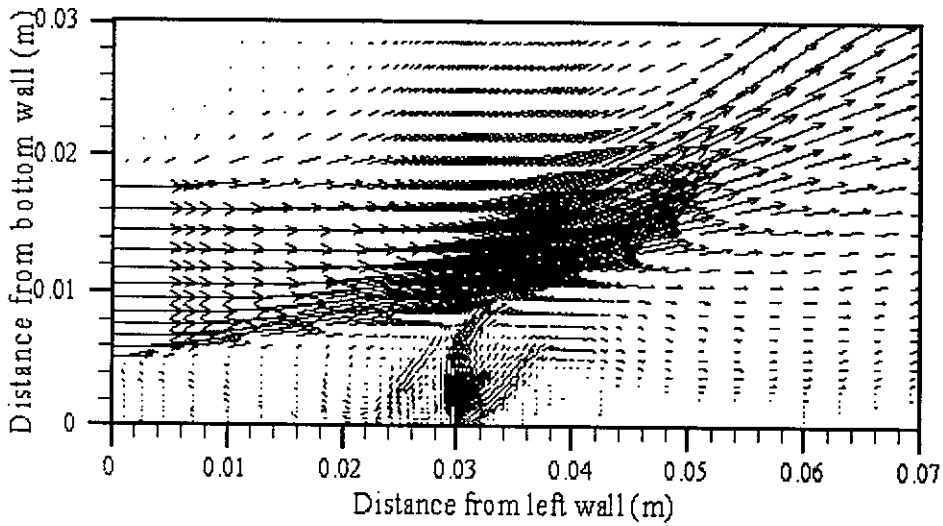
Fig. 3.6 (b) Velocity vector near injector; Case-6 ($\theta = 60^0$)
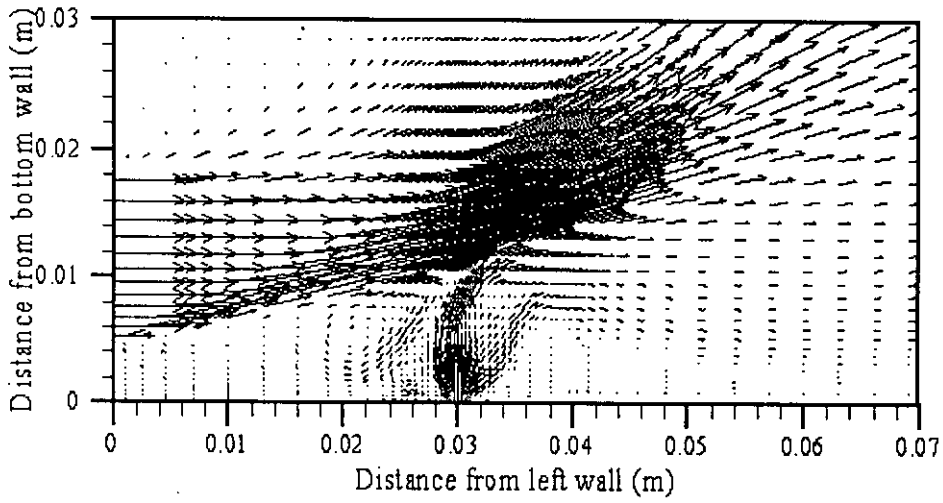
Fig. 3.6 (c) Velocity vector near injector; Case-7 ($\theta = 90^0$)
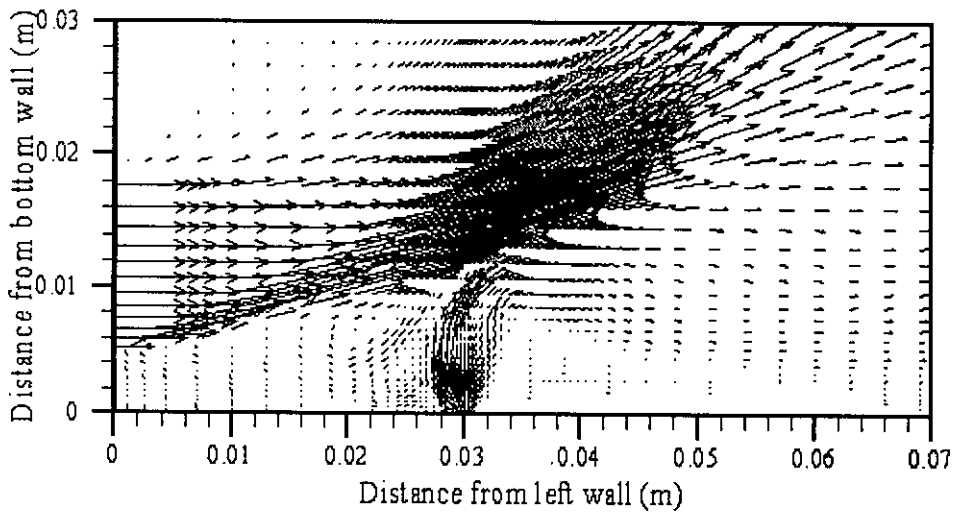
Fig. 3.6 (d) Velocity vector near injector; Case-8 ($\theta = 120^0$)
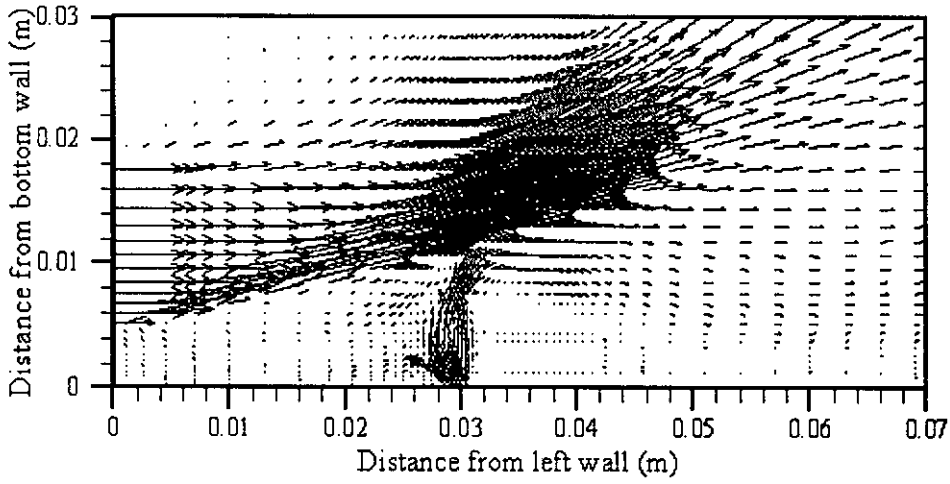
Fig. 3.6 (e) Velocity vector near injector; Case-9($\theta = 150^0$)
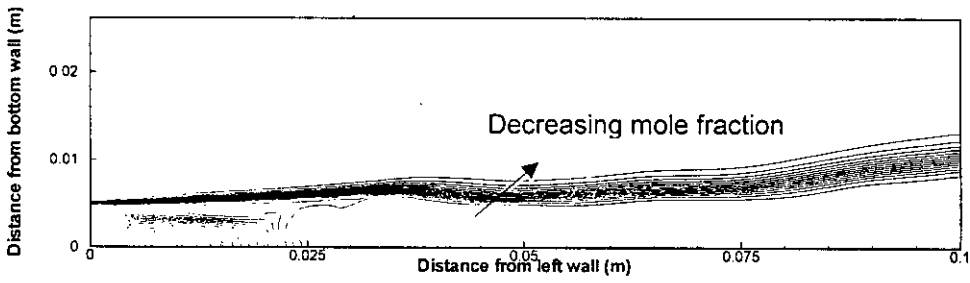
Fig. 3.7(a) Mole fraction counter of Hydrogen, $\Phi(0.05, 1.0, 0.05)$; Case-5($\theta=30°$)
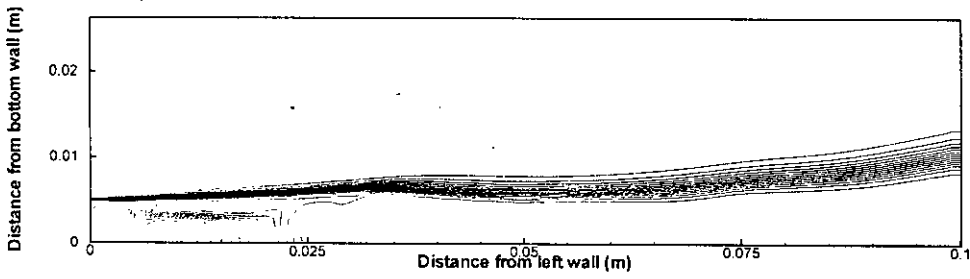
Fig. 3.7(b) Mole fraction counter of Hydrogen, $\Phi(0.05, 1.0, 0.05)$; Case-6($\theta=60°$)
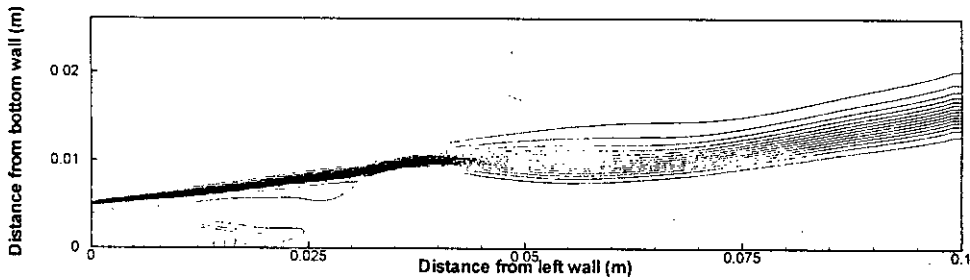
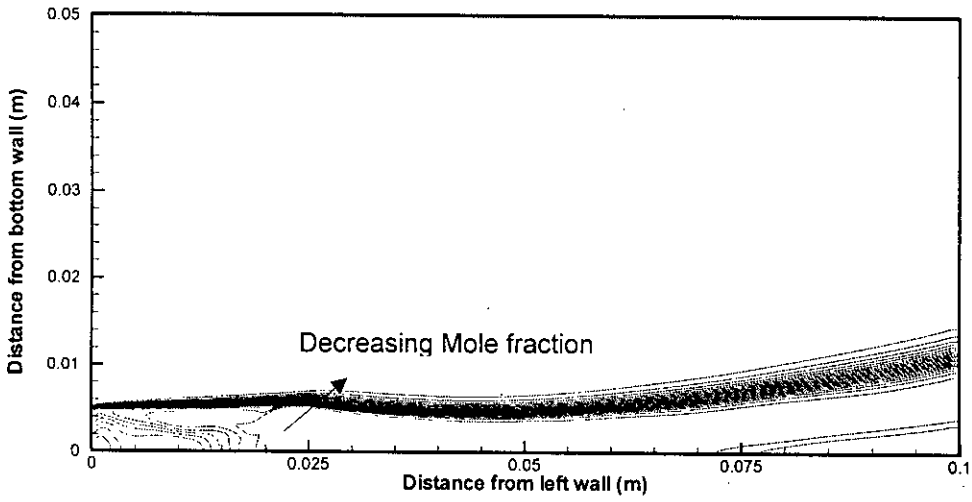Fig. 3.7(c) Mole fraction counter of Hydrogen, $\Phi(0.05, 1.0, 0.05)$; Case-7($\theta=90°$)
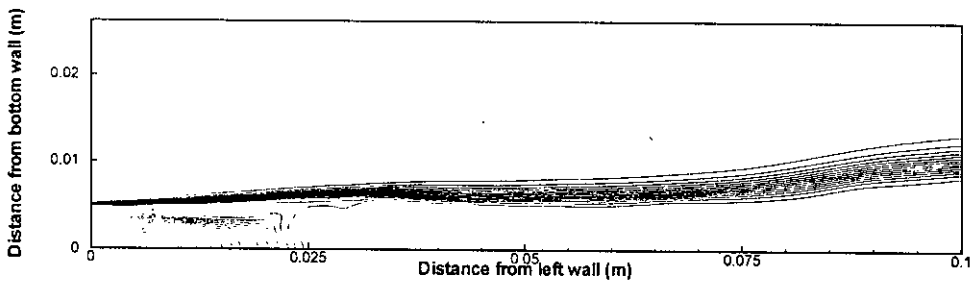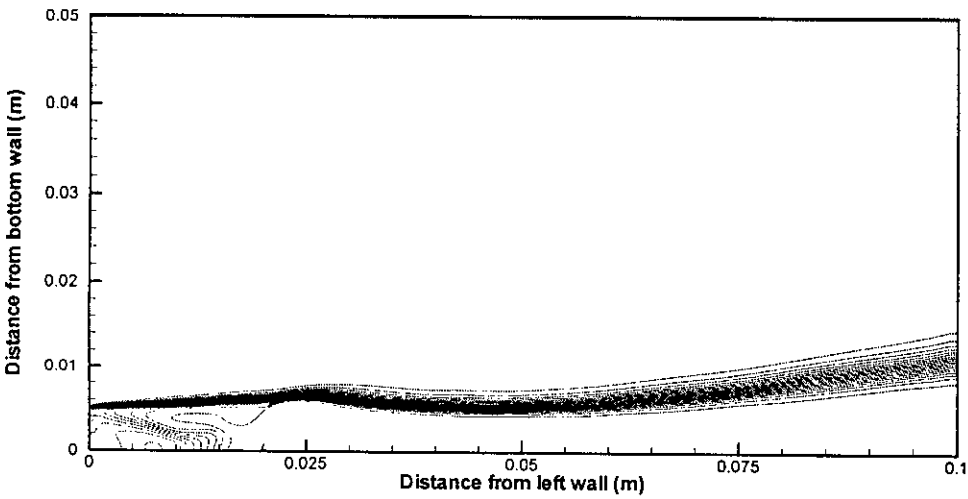
Fig. 3.7(d) Mole fraction counter of Hydrogen, $\Phi(0.05, 1.0, 0.05)$; Case-8($\theta=120°$)
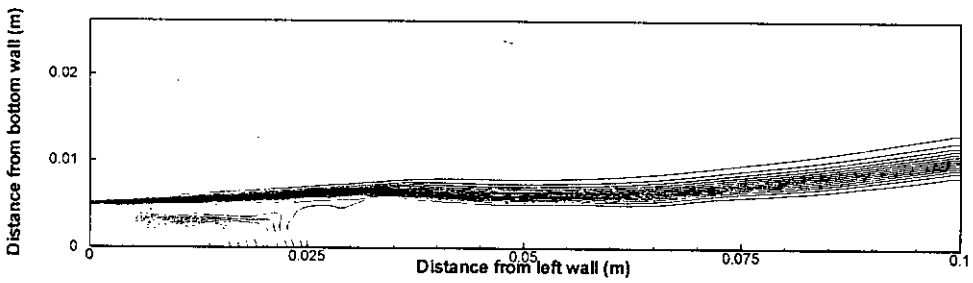
Fig. 3.7(e) Mole fraction counter of Hydrogen, $\Phi(0.05, 1.0, 0.05)$; Case-9($\theta=150°$)
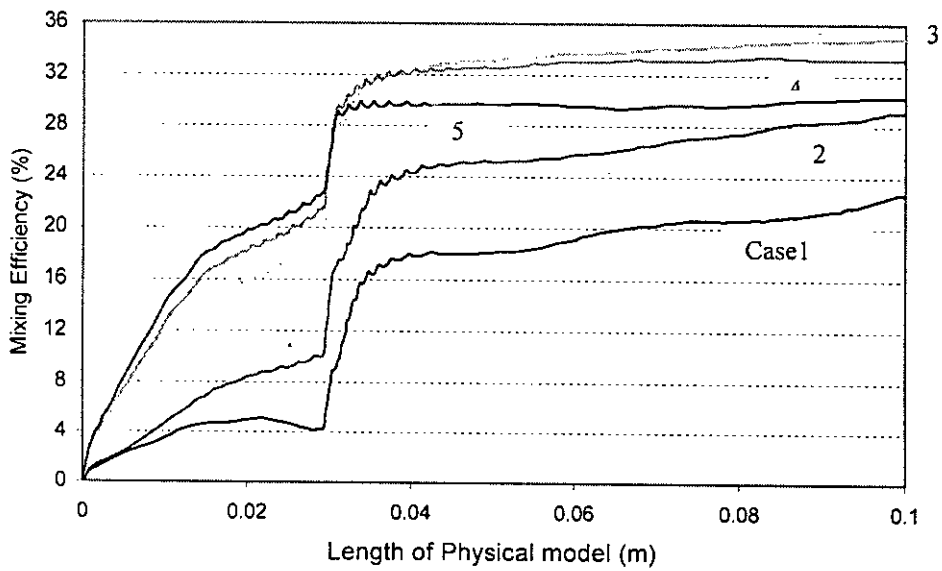
Fig.3.8 Mixing efficiency along the length of physical model

45
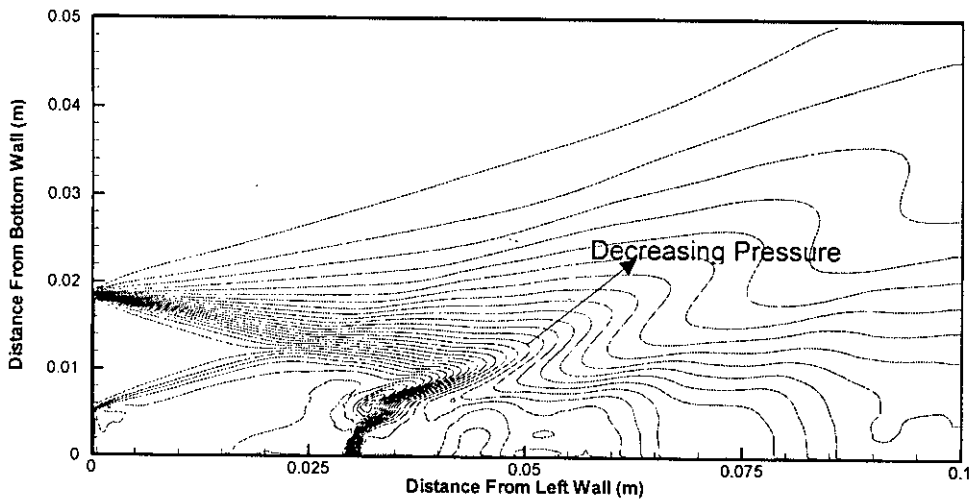
Fig. 3.9(a) Pressure (Pa) contour, $\Phi(2*10^4, 2*10^6, 2*10^4)$; Case-5($\theta$=30°)
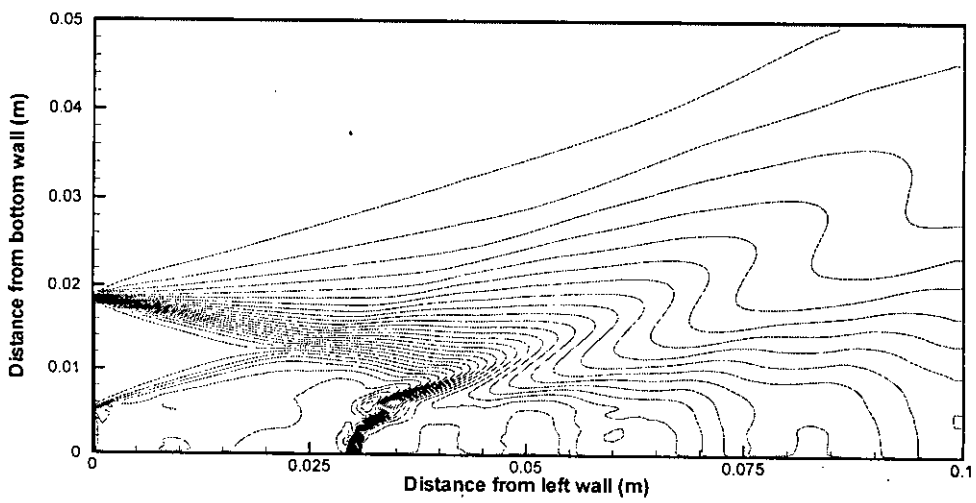
Fig. 3.9(b) Pressure (Pa) contour, $\Phi(2*10^4, 2*10^6, 2*10^4)$; Case-6($\theta$=60°)
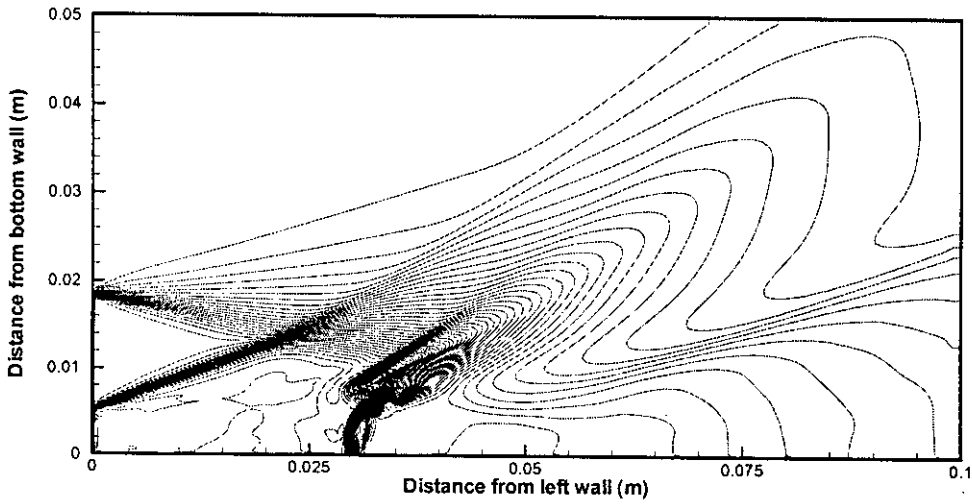
Fig. 3.9(c) Pressure (Pa) contour, $\Phi(2*10^4, 2*10^6, 2*10^4)$; Case-7($\theta$=90°)
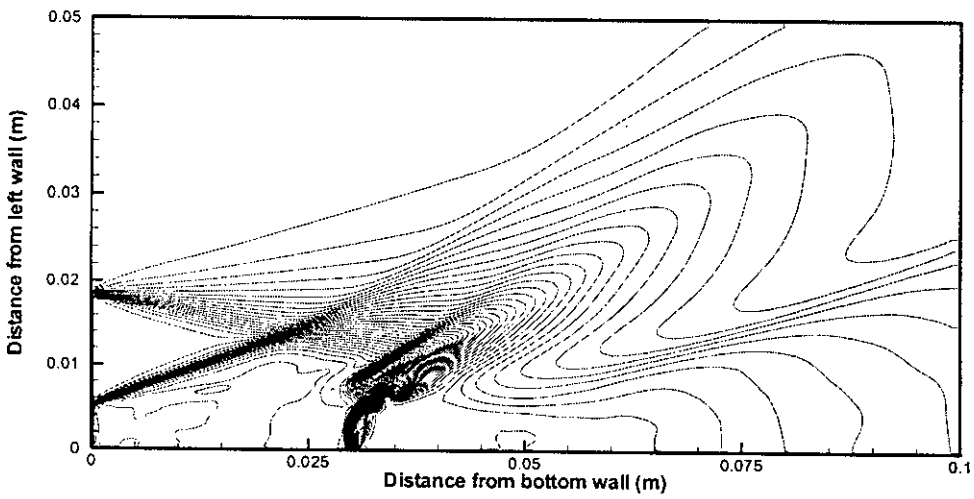
Fig. 3.9(d) Pressure (Pa) contour, $\Phi(2*10^4, 2*10^6, 2*10^4)$; Case-8($\theta$=120°)
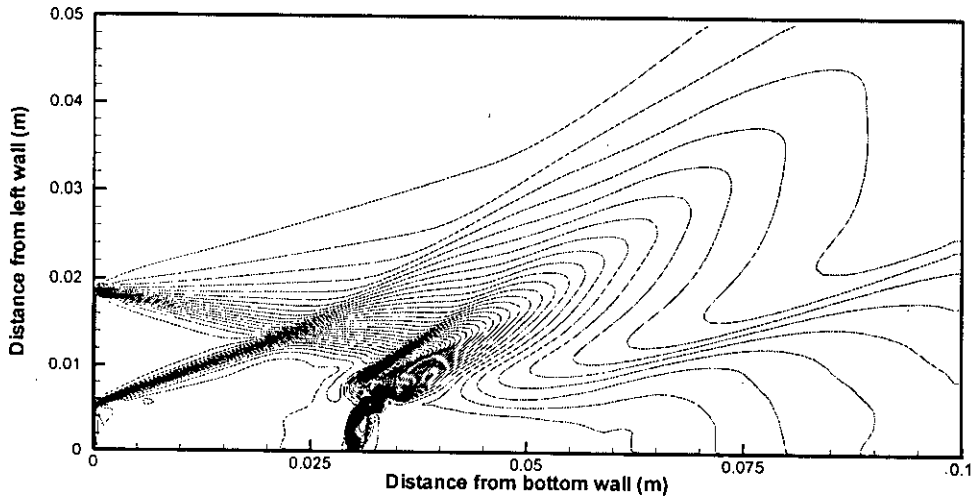
Fig. 3.9(e) Pressure (Pa) contour, $\Phi(2*10^4, 2*10^6, 2*10^4)$; Case-9($\theta=150°$)

Fig. 3.10(a) Temperature (K) contour, $\Phi(250, 2550, 100)$; Case-5($\theta=30°$)

Fig. 3.10(b) Temperature (K) contour, Φ(250, 2550, 100); Case-6(θ=60°)

Fig. 3.10(c) Temperature (K) contour, Φ(250, 2550, 100); Case-7(θ=90°)

49
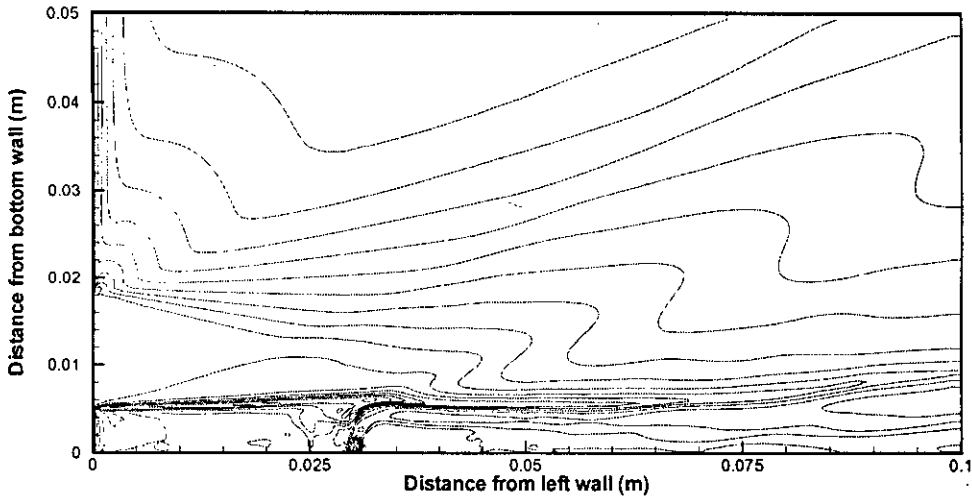
Fig. 3.10(d) Temperature (K) contour, $\Phi(250, 2550, 100)$; Case-8($\theta=120°$)
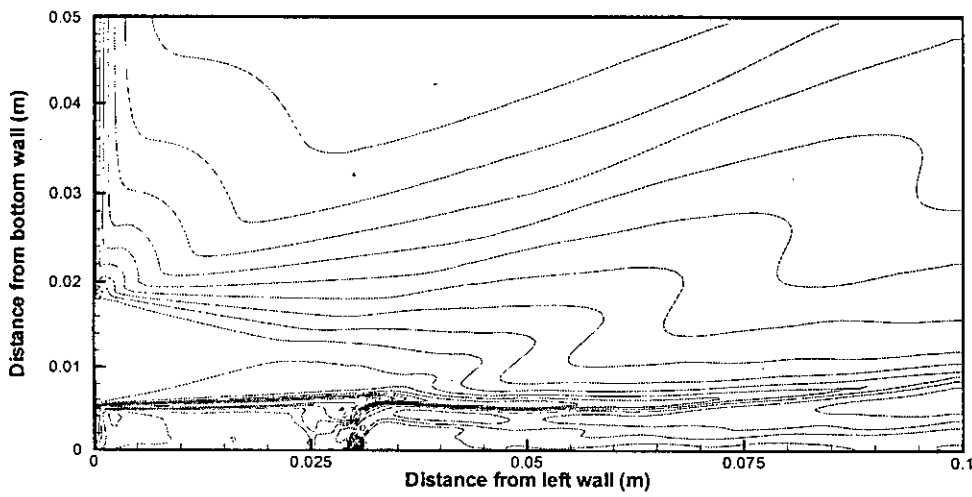
Fig. 3.10(e) Temperature (K) contour, $\Phi(250, 2550, 100)$; Case-9($\theta=150°$)

Fig.3.11(a) Mole fraction counter of Hydrogen, Φ(0.05, 1.0, 0.05) , Case-10(Mach No. = 3, d=20mm)

Fig. 3.11(b) Mole fraction counter of Hydrogen, Φ(0.05, 1.0, 0.05) , Case-11(Mach No. = 3.25, d=20mm)
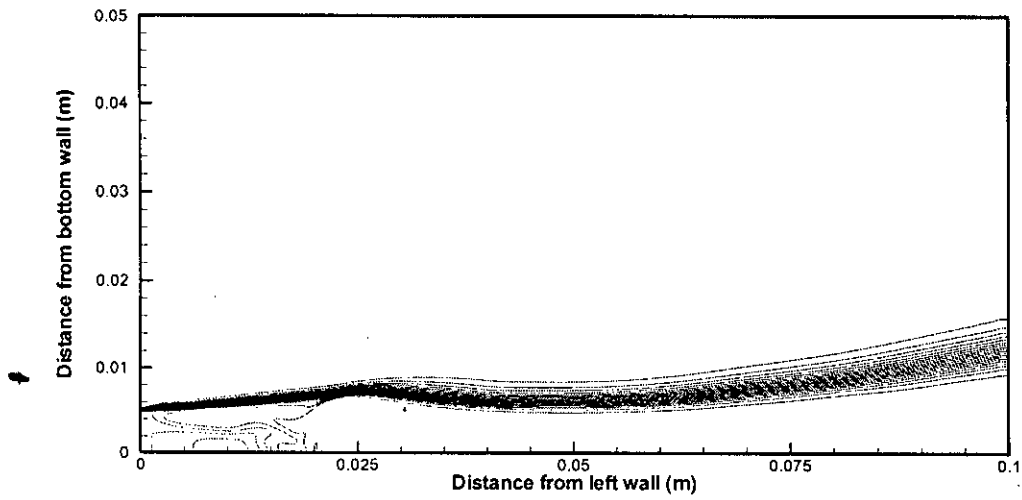
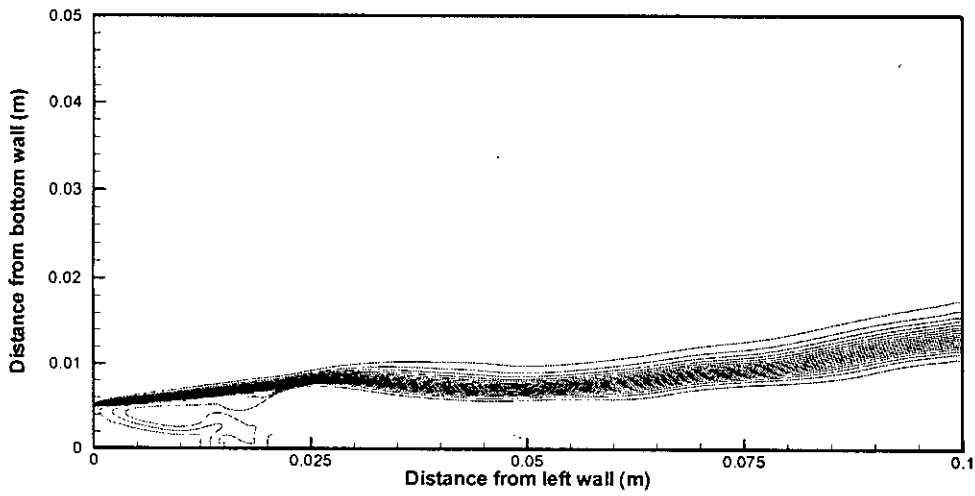Fig. 3.11(c) Mole fraction counter of Hydrogen, $\Phi(0.05, 1.0, 0.05)$, Case-12(Mach No. = 3.5, d=20mm)

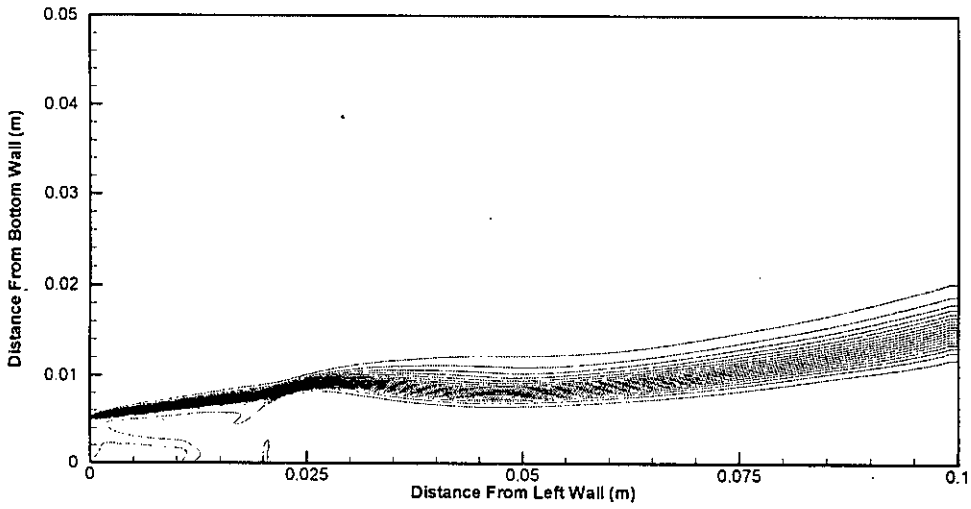Fig. 3.11(d) Mole fraction counter of Hydrogen, $\Phi(0.05, 1.0, 0.05)$, Case-13(Mach No. = 3.75, d=20mm)

Fig. 3.11(e) Mole fraction counter of Hydrogen, $\Phi(0.05, 1.0, 0.05)$; Case-14(Mach No. = 4, d=20mm)

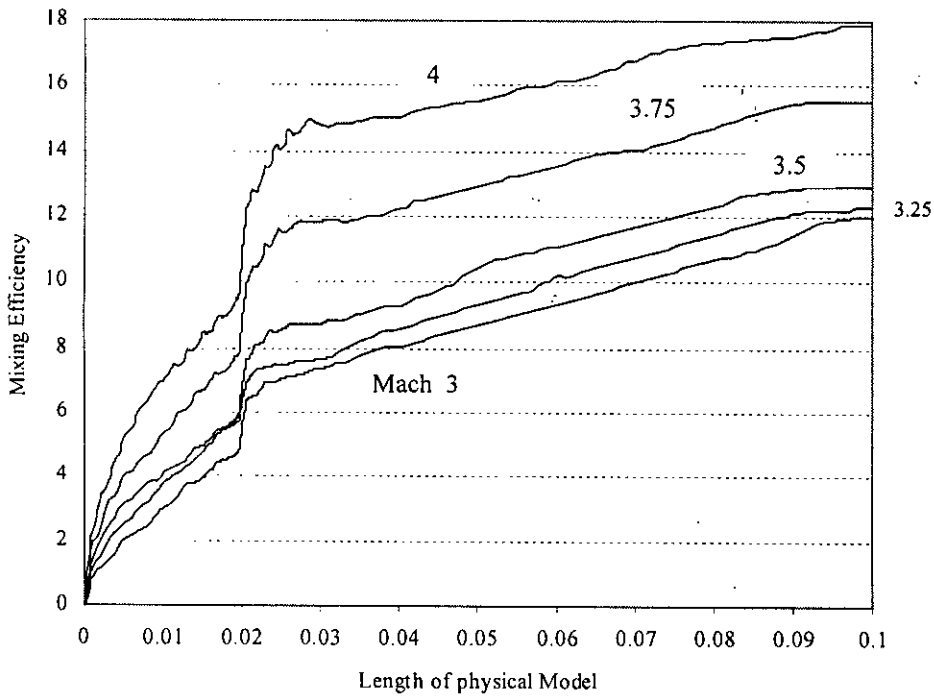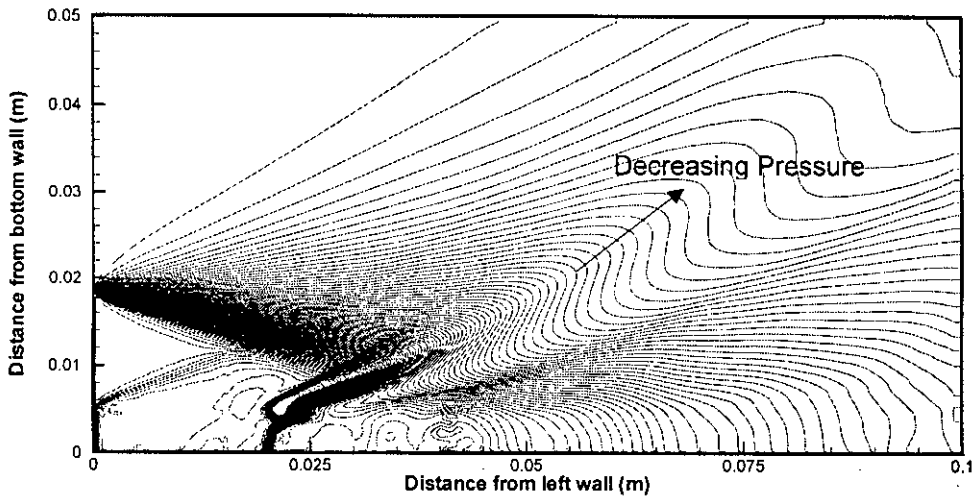Fig. 3.12 Mixing efficiency along the length of physical model

53

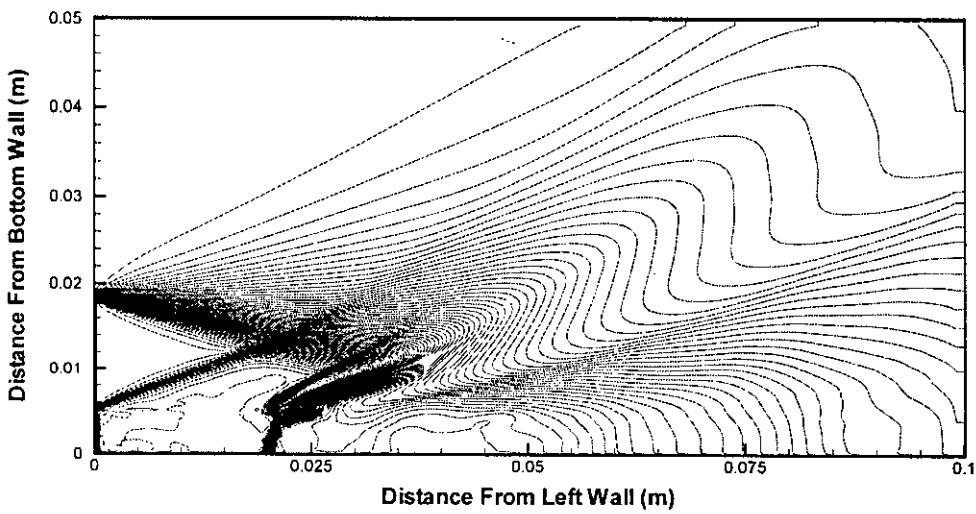Fig. 3.13(a) Pressure (Pa) contour, $\Phi(2*10^4, 2*10^6, 2*10^4)$; Case-10(Mach No. = 3, d=20mm)

Fig. 3.13(b) Pressure (Pa) contour, $\Phi(2*10^4, 2*10^6, 2*10^4)$; Case-11(Mach No. = 3.25, d=20mm)
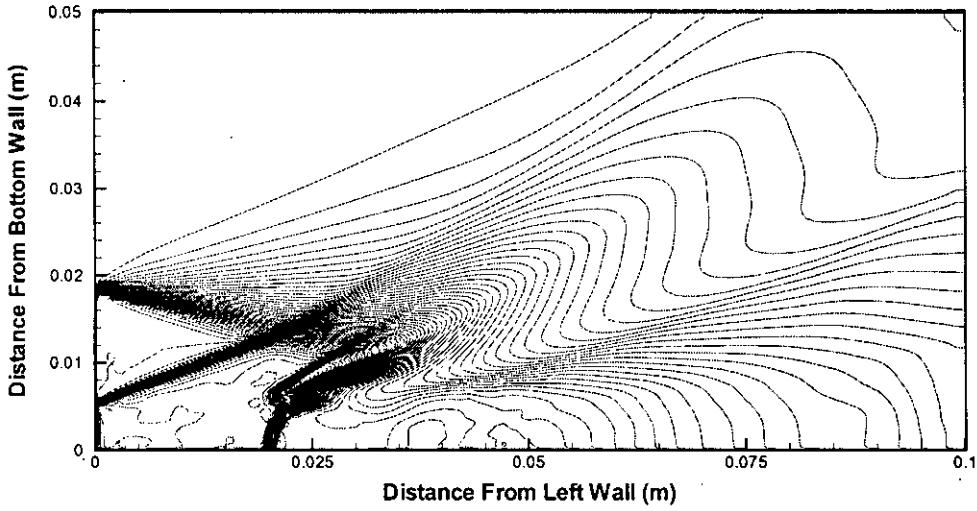
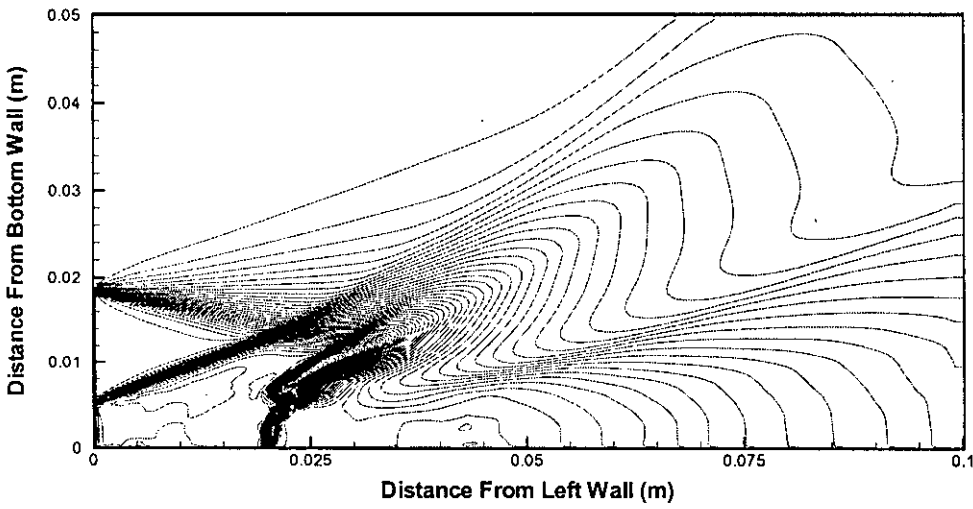Fig. 3.13(c) Pressure (Pa) contour, $\Phi(2*10^4, 2*10^6, 2*10^4)$; Case-12(Mach No. = 3.5, d=20mm)

Fig. 3.13(d) Pressure (Pa) contour, $\Phi(2*10^4, 2*10^6, 2*10^4)$; Case-13(Mach No. = 3.75, d=20mm)
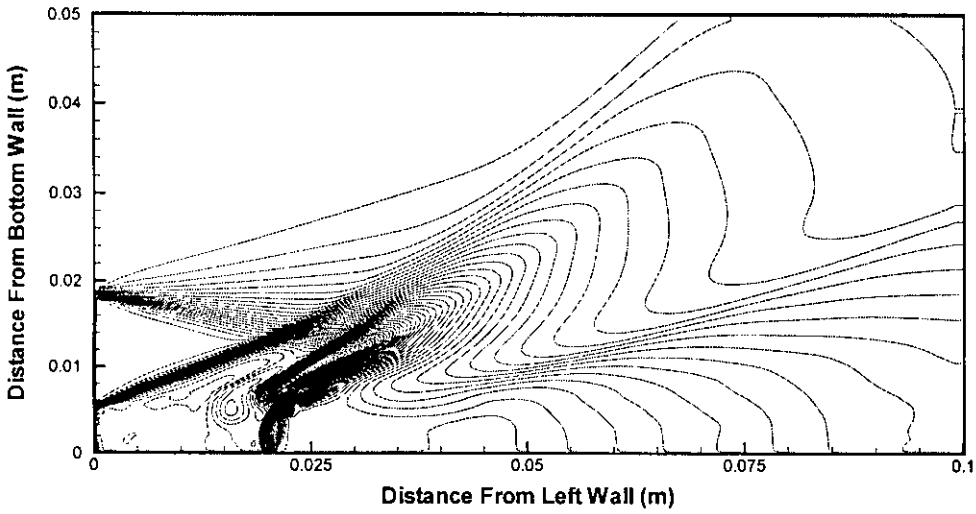
Fig 3.13(e) Pressure (Pa) contour, $\Phi(2*10^4, 2*10^6, 2*10^4)$; Case-14(Mach No. = 4, d=20mm)

Fig. 3.14(a) Temperature (K) contour, $\Phi(250, 2550, 100)$; Case-10(Mach No. = 3, d=20mm)

Fig. 3.14(b) Temperature (K) contour, Φ(250, 2550, 100); Case-11(Mach No. = 3.25, d=20mm)

Fig. 3.14(c) Temperature (K) contour, Φ(250, 2550, 100); Case-12(Mach No. = 3.5, d=20mm)

57
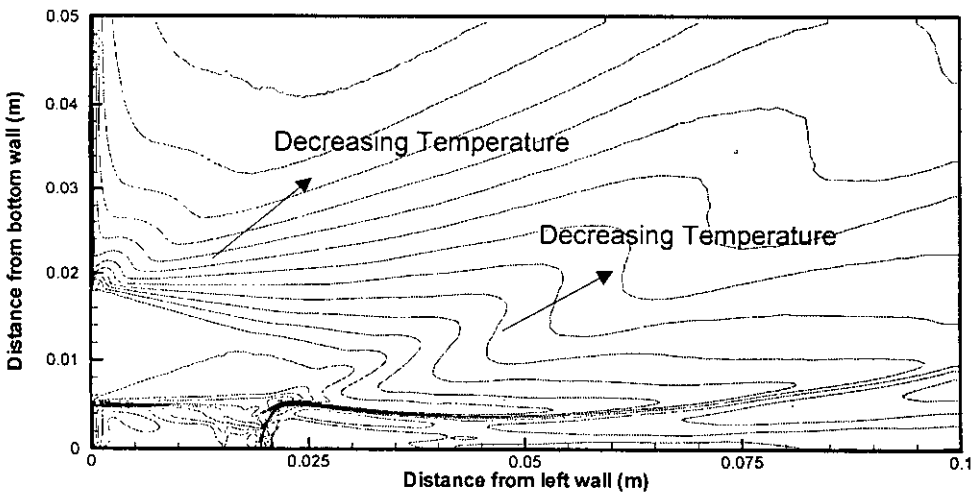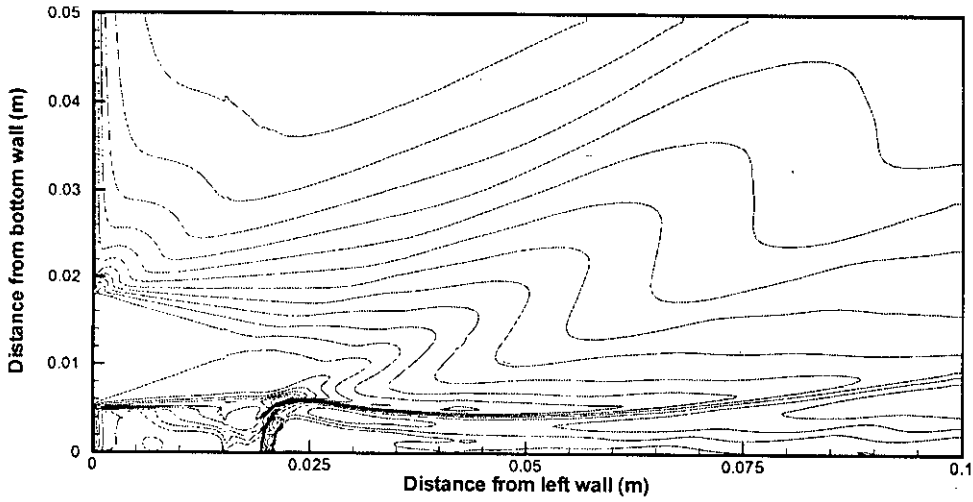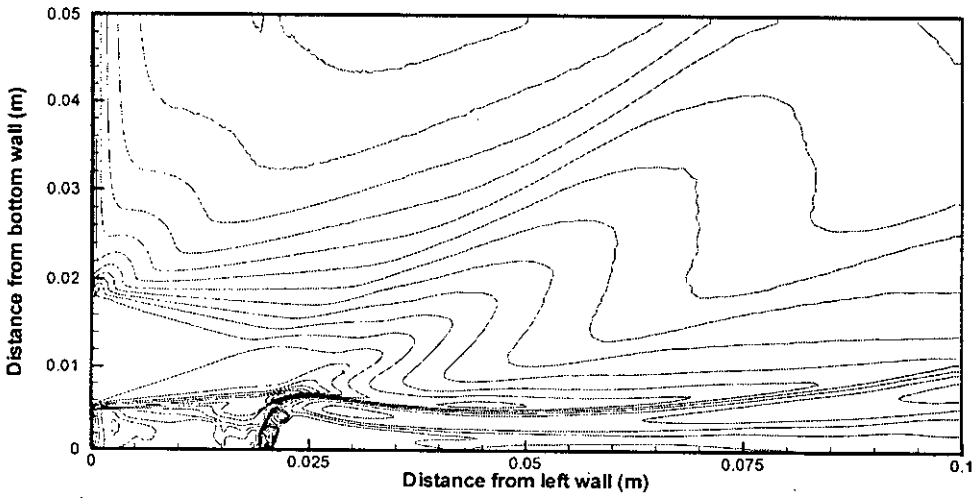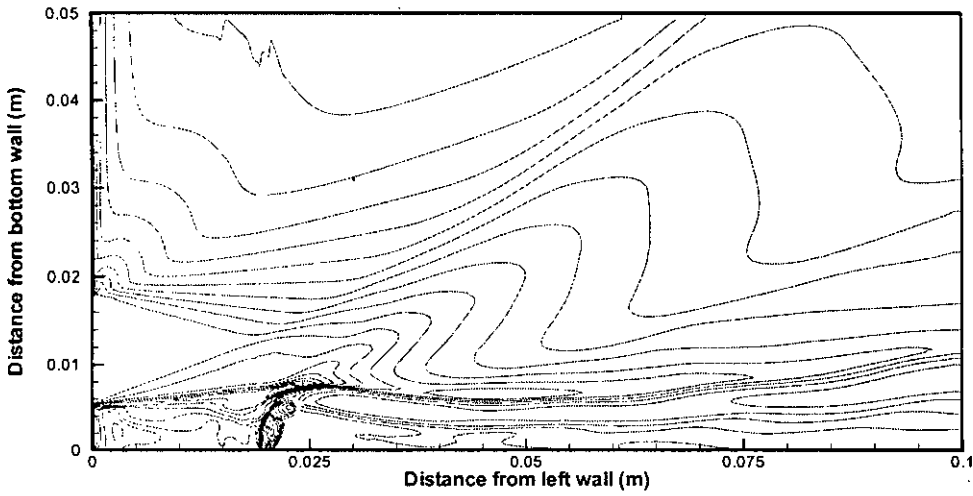
Fig. 3.14(d) Temperature (K) contour, $\Phi(250, 2550, 100)$; Case-13(Mach No. = 3.75, d=20mm)
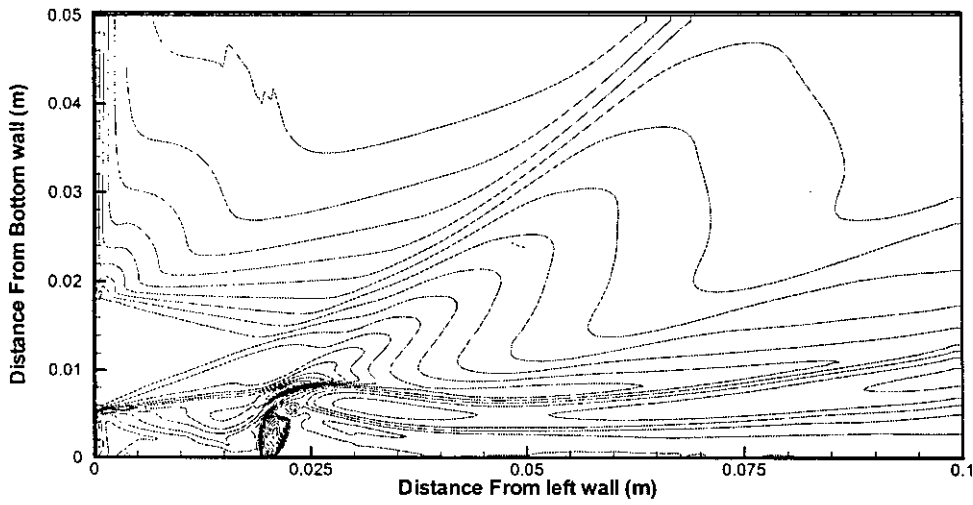

Fig. 3.14(e) Temperature (K) contour, $\Phi(250, 2550, 100)$; Case-14(Mach No. = 4, d=20mm)

BIBLIOGRAPHY

[1]   Brown, G. L. and Roshko, A.: On Density Effects and Large Structure in Turbulent Mixing Layer, *J. Fluid Mechanics,* Vol. 64, No. 4, pp.775-816, (1974).

[2]   Papamoschou, D. and Roshko, A.: Observation of Supersonic Free Shear Layers, *AIAA Paper 86-0162,* January (1986).

[3]   Ragab, S. A. and Wu, J.L.: Instabilities in the Free Shear Layer Formed by Two Supersonic Streams, *AIAA Paper 88-0038,* January, 1988.

[4]   Rogers, R. C.: A Study of the Mixing of Hydrogen Injected Normal to a Supersonic Airstream, *NASA TN D-6114,* (1971).

[5]   Kraemer, G. O. and Tiwari, S. N.: Interaction of Two-Dimensional Transverse Jet with a Supersonic Mainstream, *NASA CR 175446,* (1983).

[6]   Holdeman, J. D. and Walker, R. E.: Mixing of a Row of Jets with a Confined Crossflow, *AIAA Journal,* Vol. 5, no. 2, pp. 243-249, (1977).

[7]   Thayer III, W. J. and Corlett, R. C.: Gas Dynamic and Transport Phenomena in the Two-Dimensional Jet Interaction Flowfield, *AIAA Journal,* Vol. 10, pp. 488-493, (1972).

[8]   Heister, S. D., Nguyen, T. T. and Karagozian, A. R.: Modeling of Liquid Jets Injected Transversely into a Supersonic Crossflow, *AIAA Journal,* Vol. 27, no. 12, pp. 1727-1734, (1989).

[9]   Catalano, G. D., Chang, K. S. and Mathis, J. A.: Investigation of Turbulent Jet Impingement in a Confined Crossflow, *AIAA Journal,* Vol. 27, No. 11, 1989, pp. 1530-1535.

[10]   Zakkay, V., Calarese, W. and Sakell, L.: An Experimental Investigation of the Interaction between a Transverse Sonic Jet and a Hypersonic Stream, *AIAA Journal,* Vol. 9, No. 4, pp. 674-682, 1971.

[11]   Thayer III, W.J.: New Information on the Two-Dimensional Jet Interaction Problem, *AIAA Journal,* Vol. 9, No. 3, pp. 539-541, 1971.

[12]   Torrence, M.G.: Effect of Injectant Molecular Weight on Mixing of a Normal Jet in a Mach 4 Airstream, *NASA TN D-6061,* January, 1971.

[13]   Rodrizuez, G., Galametz, I., Thorembey, M.H., Rayer, C. & Haas. J.F.: Visualization of shocked mixing zones using differential interferometry and X-rays, *Proceedings of the 20th Int. Symp. on Shock Waves,* California, USA, 1995, pp. 647-652.

[14]   Zukoshi, E. E. : Turbulent Boundary Layer Separation in Front of a Forward-Facing Step, *AIAA Journal,* Vol. 5, No. 10, pp. 1746-1753, 1967.

[15]   Zukoshi, E. E. and Spaid, F.W.: Secondary Injection of Gases into a Supersonic Flow, *AIAA Journal,* Vol. 2, No. 10, 1964, pp. 1689-1696.

[16]   Weidner, E.H. and Drummond, J.P.: A Parametric Study of Staged Fuel Injector Configurations for Scramjet Applications, *AIAA Paper 81-11468,* (1981).

[17]   Takahashi, M. and Hayashi, A.K.: Numerical Study on Mixing and Ignition of Injecting Jet into a Supersonic Flow, *Proc. of Int. Symp. on Comp. Fluid Dynamics,* Nagoya, pp. 465-470, August, 1989.

[18]   Spaid, F. W. and Zukoshi, E. E.: A Study of the Interaction of Gaseous Jets from Transverse Slots with Supersonic External Flows, *AIAA Journal,* Vol. 6, No. 2, pp. 205-212, 1968.

[19]   Yokota, K. and Kajii, S.: The Three-Dimensional Supersonic Flow and Mixing Fields with a Perpendicular Air Injection from a Finite Length Slit, *Trans. Japan Soc. Aero. Space Sci.,* Vol. 39, no. 124, pp. 173-183, (1996).

[20]   Yokota, K. and Kajii, S.: The Effects of Aspect Ratio of a Finite Length Slit on the Mixing in the Three-Dimensional Supersonic Flow, *Trans. Japan Soc. Aero. Space Sci.,* Vol. 39, no. 124, pp. 199-210, (1996).

[21]   Yokota, K. and Kajii, S.: The Injection Methods and Mixing Characteristics in the Two-Dimensional Supersonic Free Stream, *Trans. Japan Soc. Aero. Space Sci.,* Vol. 38, no. 122, pp. 383-393, (1996).

[22]   Yokota, K. and Kaji, S.: The Two Dimensional Supersonic Flow and Mixing Field with a Perpendicular Injection, *Trans. Japan Soc. Aero. Space Sci.,* Vol. 39, No. 123, pp. 28-42, 1996.

[23]   Yoshida, A. and Tsuji, H.: Supersonic Combustion of Hydrogen in a Vitiated Airstream Using Transverse Injection, *AIAA Journal,* Vol. 15, No. 4, pp. 463-464, 1977.

[24] Crabb, D., Durao, D.F.G. and Whitelaw, J.H.: A Round Jet Normal to a Crossflow, *J. Fluids Engg.*, Vol. 103, pp. 142-153, 1981.

[25] Drummond, J.P. and Weidner, E.H.: Numerical Study of a Scramjet Engine Flow Field, *AIAA Paper 81-0186*, January, 1981.

[26] Nakae, T., Teramoto, S. and Nagashima, T.: DSMC Method for Transverse Gas Ignition into a Supersonic Air Flow, Air Flow, *Eleventh International Symposium on Air Breathing Engines*, Tokyo, Japan, pp. 728-733, September 1993.

[27] Obata, S. and Nagashima, T.: Direct Simulation of Reacting Fuel Gas Flows in a Supersonic Mixing Layer, *Eleventh International Symposium on Air Breathing Engines*, Tokyo, Japan, pp. 739-745, September, 1993.

[28] Kumar, A. Bushnell, D. M. and Hussaini, M.Y.: A Mixing Augmentation Technique for Hypervelocity Scramjets, *AIAA Paper 87-1882*, June, 1987.

[29] Guirguis, R.H.: Mixing Enhancement in Supersonic Shear Layers: Effect of Convective Mach Number, *AIAA Paper 88-0701*, January, 1988.

[30] Orth, R.C., Schetz, J.A. and Billig, F.S.: The Interaction and Penetration of Gaseous Jets in Supersonic Flow, *NASA CR-1986*.

[31] Moussa, Z. M., Trischka, J.W. and Eskinazi, S.: The Near Field in the Mixing of a Round Jet with a Cross-Stream, *J. Fluid Mechanics*, Vol. 80, Par-1, pp. 49-80, 1977l.

[32] Andreopulous, J. and Rodi, W.: Experimental Investigation of Jets in a Crossflow, *J. Fluid Mechanics*, Vol. 138, pp. 93-127, 1984.

[33] Andreopoulos, J.: On the Structure of Jets in a Crossflow, *J. Fluid Mechanics*, Vol. 157, pp. 163-197, 1985.

[34] Anderson, Jr. J. D.: Hypersonic and High Temperature Gas Dynamics, McGraw-Hill Book Company, New York, pp. 592-605, 1989.

[35] Moss, J. N.: Reacting Viscous-Shock-Layer Solutions with Multicomponent Diffusion and Mass Injection, *NASA TR-411*, June 1974.

[36] White, F.M.: *Viscous Fluid Flow*, McGraw-Hill, New York, (1974).

[37] Brokaw, R.S.: Alignment Charts for Transport Properties Viscosity, Thermal Conductivity, and Diffusion Coefficients for Nonpolar Gases and Gas Mixtures at Low Density, *NASA TR R-81*, 1961.

[38] Reid, R.C. and Sherwood, T.K.: *The Properties of Gases and Liquids,* Second Edition, McGraw-Hill, New York, pp. 520-543, (1966).

[39] Yee, H.C.: A Class of High-Resolution Explicit and Implicit Shock Capturing Methods, *NASA, TM 101088,* (1989).

[40] Ali, M.: Physics of Supersonic Mixing and Combustion of a Transverse Jet in Two-Dimensional Finite Stream, Ph.D. Dissertation, Department of Aerospace Engineering, Nagoya University, Japan, March, 1998.

[41] Ali, M., Fujwara, T. and Leblance J. E.: "The Effects of Backward-facing step on Mixing and Flame holding in Supersonic Combustor, Journal of Energy, Heat and Mass Transfer, Vol. 23, pp.319-338, 2001.

[42] Rausch,V.L., McClinton, C.R. and Hicks, J.W.: Scramjet Breath New Life into Hypersonics, *Aerospace America,* July (1997).

[43] Ali, M. and Islam, A.K.M.S.: Effect of Mainflow Inlet Width on Penetration and Mixing of Hydrogen in Scramjet Combustor, *Proceedings of the Eighth Asian Congress of Fluid Mechanics,* pp. 647–650, December 6-10, Shenzhen, China, (1999).

[44] Tabejamaat, S. JU. Y. and Niioka, T.: Numerical Simulation of Secondary Combustion of Hydrogen Injected from Preburner into Supersonic Airflow, *AIAA Journal,* Vol.35, no.9,September, (1997).